Buckling transitions and soft-phase invasion of two-component icosahedral shells

Emanuel, Marc D.; Cherstvy, Andrey G.; Metzler, Ralf; Gompper, Gerhard

DOI
10.1103/PhysRevE.102.062104

Publication date
2020

Document Version
Final published version

Published in
Physical Review E

Buckling transitions and soft-phase invasion of two-component icosahedral shells

Marc D. Emanuel,[1,2] Andrey G. Cherstvy,[1,3] Ralf Metzler,[3] and Gerhard Gompper[1]
[1]*Theoretical Physics of Living Matter, Institute of Biological Information Processing, Forschungszentrum Jülich GmbH, 52425 Jülich, Germany*
[2]*Kavli Institute for Nanoscience, Technical University Delft, 2628 CJ Delft, Netherlands*
[3]*Institute for Physics & Astronomy, University of Potsdam, 14476 Potsdam-Golm, Germany*

(Received 25 July 2020; revised 12 October 2020; accepted 11 November 2020; published 2 December 2020)

What is the optimal distribution of two types of crystalline phases on the surface of icosahedral shells, such as of many viral capsids? We here investigate the distribution of a thin layer of soft material on a crystalline convex icosahedral shell. We demonstrate how the shapes of spherical viruses can be understood from the perspective of elasticity theory of thin two-component shells. We develop a theory of shape transformations of an icosahedral shell upon addition of a softer, but still crystalline, material onto its surface. We show how the soft component "invades" the regions with the highest elastic energy and stress imposed by the 12 topological defects on the surface. We explore the phase diagram as a function of the surface fraction of the soft material, the shell size, and the incommensurability of the elastic moduli of the rigid and soft phases. We find that, as expected, progressive filling of the rigid shell by the soft phase starts from the most deformed regions of the icosahedron. With a progressively increasing soft-phase coverage, the spherical segments of domes are filled first (12 vertices of the shell), then the cylindrical segments connecting the domes (30 edges) are invaded, and, ultimately, the 20 flat faces of the icosahedral shell tend to be occupied by the soft material. We present a detailed theoretical investigation of the first two stages of this invasion process and develop a model of morphological changes of the cone structure that permits noncircular cross sections. In conclusion, we discuss the biological relevance of some structures predicted from our calculations, in particular for the shape of viral capsids.

DOI: 10.1103/PhysRevE.102.062104

I. INTRODUCTION

Geometrically ideal closed three-dimensional surfaces, starting from the Platonic solids [1], have inspired many thinkers and scientists over centuries and millennia. The inherent stability of such polyhedral shells constructed from jointed triangular subunits has influenced some famous architects, such as Buckminster Fuller with his visionary geodesic domes [2,3]. The name "Buckminster fullerene" was coined for C_{60} "buckyballs" discovered by Kroto *et al.* [4,5] and composed of $n_C = 60$ carbon atoms connected into a shell with 60 vertices and 32 faces (with 12 pentagonal and 20 hexagonal faces) [8]. Small fullerenes have a soccer-ball appearance, possessing the symmetry group of truncated icosahedra [6], while large fullerenes are polyhedrally faceted [7,8] (see Sec. IV C).

Polyhedral shells also describe the geometric shape of many spherical viruses very well [9]. The energetics, thermodynamics, and kinetics of quite elaborate physical-chemical processes involved in the mechanisms of viral-capsid stability and (self-) assembly have been the subject of intense research over the last decades by different scientific communities (the list of studies is too long to properly overview it here).

Our main objective is to advance the theoretical understanding of the energetics of icosahedral shells, including those composed of two different crystalline materials having a nonzero line tension between them. We start with a general overview of topological defects and the energetics of shells, including icosahedra (Sec. I A), continue with the physics of buckling transitions (Sec. I B), and discuss the recent advances for the two-component shells in Sec. I C. We note here that experts may directly jump to Sec. II B, while standard readers may find useful the general introduction provided below.

A. One-component shells: Icosahedra, topological defects, and physical properties of viral capsids

The phenomenon of wrapping of a hexagonally symmetric crystalline planar sheet onto a spherical surface is accompanied by creation of (at least) 12 innate topological defects [10–12,15]: these disclinations are singular points with no sixfold symmetry [13,14,16–20]. It follows from the topological invariance of the Euler characteristics χ_E (the alternating sum of the number of vertices $n_{\rm vert}$, edges or ridges $n_{\rm edge}$, and faces $n_{\rm face}$) that for a *closed* polyhedral surface isomorphic to a sphere is [8]

$$\chi_E = n_{\rm vert} - n_{\rm edge} + n_{\rm face} = 2. \tag{1}$$

Disclinations have typically a fivefold symmetry and absorb the stretching energy to be paid upon surface wrapping. Elasticity-mediated repulsion between the defects on a hexagonal lattice [14], in analogy to the Thompson problem in classical electrostatics [21–23], distributes the defects for a hardly stretchable but easily bendable membranous material

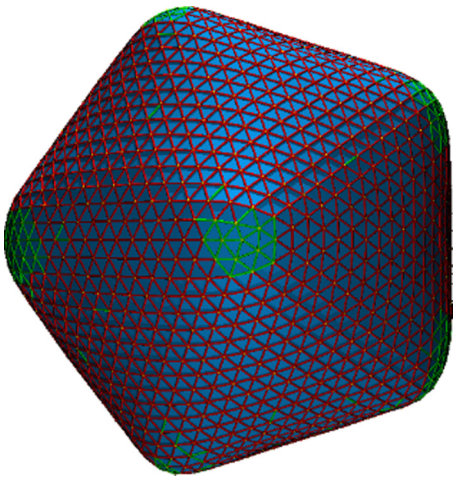

FIG. 1. Structure of a rigid crystalline icosahedral shell with the vertices "invaded" by the soft material (the image courtesy of Vliegenthart, unpublished). The triangulated lattice mesh of the rigid and soft materials is shown in magenta red and green colors, respectively.

at the vertices of the icosahedron (see Fig. 1). In this figure, the triangulated lattice of the crystalline material in a closed icosahedrally symmetric shell imposes mostly the bending-energy penalty on the edges; it also experiences bending- and stretching-energy-associated penalties at the 12 vertices.

Icosahedral shapes, abundant in physics and crystallography [24], are known to minimize the elastic energy of the ridges. One biological example are the surfaces of bacteriophage capsids [25,26] and spherical viruses [9,27–45]. As predicted by Crick and Watson [34], the capsids are constructed from protein subunits of a small molecular weight (often chemically identical or consisting of a few distinct types). The viral capsids follow the principle of quasiequivalence for the subunit-subunit interaction environments, as established by Caspar and Klug [35] and yield energy-optimized structures (see Sec. III B). The faces of icosahedral capsids often have hexagonal symmetry of protein subunits, while the vertices have pentagonal symmetry [9,37,38]. In doing so, virus capsids reduce the penalties for the formation of 12 defects at the icosahedron's vertices (if formed from the planar protein sheet having the lowest-energy state as a equitriangulated, sixfold-symmetric lattice). We refer also to Refs. [43,46–59] for the nanoindentation of virus capsids and to Ref. [54] for a comparative analysis of elastic moduli and their variability among viral families.

The shape, self-assembly, and energetic stability of the generic icosahedra were rationalized in a large number of theoretical [18,23,33,38,60–79], computer-simulations-based [15,80–97], and experimental [25,98,100–113] studies [114]. From the perspective of viral-capsid self-assembly (see Refs. [75,82,102–105] for oligomerization-based kinetic and thermodynamic theories), a number of RNA-containing virus families (see, e.g., Ref. [28] for an extensive review) form their virions via a simultaneous packing of the genetic material, surrounding and stabilizing it by capsid proteins [75,115–117].

B. Buckling transitions: Mathematical approach and summary of classical results

Mathematically, based on the elasticity theory of thin sheets and Föppl–von Kármán (FvK) equations [121–123], the energetics of the defect-driven buckling transition of crystalline shells was examined in Refs. [17,18,124,125]. The scaling laws for energy focusing in the ridges of these structures were derived by Witten and coworkers [19,126–135] (see also Refs. [136–141]). The FvK equations for thin elastic shells were solved using a mesh discretization for model polymerized membranes [142]. Other examples of ridge formation and buckling include crumpling of paper [143–147] and other materials [148–150]. Wrinkles are also formed on thin elastic membranes [19,151–155], on polymer films and surfaces [156–159], in wrapped geometries [160], on soft spherical vesicles [20,161,162], on pollen grains [163], and on graphene sheets [164,165], to mention a few physical examples [166].

The elastic energy of a buckled (positive) disclination [17] has been estimated by matching the two extreme cases: a flat disk around it with only in-plane stresses (with the energy growing with the area) and a stretch-free cone (with the bending energy growing logarithmically) (see the seminal studies of Nelson and coworkers [17,18]). Specifically, the solution of the biharmonic equation

$$\nabla^4 \chi(r) = sK\delta(r) \tag{2}$$

for the Airy stress function $\chi(r)$ with the defect "charge"

$$s = 2\pi/6 \tag{3}$$

for a flat disk was obtained in Ref. [17]. Here, K is the two-dimensional Young's modulus. The stretching energy of a defect grows quadratically with the radius of the disk R,

$$E_{\rm str}(R) = Ks^2R^2/(32\pi), \tag{4}$$

while the bending energy of a stress-free buckled cone grows logarithmically [14,17,18,84],

$$F_{\rm bend}(R) = s\kappa \, \log(R/R_b), \tag{5}$$

with κ being the bending modulus (measured in units of thermal energy k_BT).

The buckling transition can be understood via a competition between the strain-favoring localization of the Gaussian curvature [169] around the defects and the bending energy that prefers to spread the mean curvature over the surface. The dimensionless FvK number [17,18],

$$\gamma = KR^2_{\rm shell}/\kappa, \tag{6}$$

describes the degree of shell "buckleness." Here, $R_{\rm shell}$ is the radius of a sphere with the *same area* as the icosahedron. This is the so-called constant-surface constraint; we refer also to the constant-volume calculations for the buckling transition of icosahedra considered in Ref. [68]. Many convex icosahedral viral capsids indeed pronouncedly buckle outwards as their radius grows [9] and the respective FvK numbers exceed the theoretically predicted critical value [17,18,84]

$$\gamma \gtrsim \gamma_b \approx 154. \tag{7}$$

Hereafter, we reserve the subscript "b" for the buckling-related quantities and observables. For larger shells and at

increasing FvK numbers the edges of the capsids additionally sharpen, as obtained from the three-dimensional (3D) reconstruction of cryoelectron-microscopy images of viral capsids [9]. The virus-related FvK numbers are [18,71]

$$\gamma \simeq 10^2 \ldots 10^3, \tag{8}$$

reaching a colossal value $\gamma \simeq 10^4$ for the giant mimivirus [40,170,171] (see Sec. IV B).

In curved spaces, generalized theories of defect formation were developed [19] and applied, *inter alia*, to the experimental data on formation of defects and grain-boundary scars [20,23,24,85,92,112,172–176]. Also, the elastic energy of ridges $E_{\rm ridge}$ was found using scaling arguments [126,132] and derived from the van Kármán equations [133,135]. The scaling exponent was found independent of the boundary conditions [135], with the ridge energy obeying the law

$$E_{\rm ridge}(\gamma) \sim \gamma^{1/6}. \tag{9}$$

C. Multicomponent crystalline shells: Optimal structures and physical systems

While one-component crystalline shells [177,178] are relatively well understood [18,19], the structure, lowest-energy states, and mechanical properties of two-component shells [84,86,179,180] present often a nontrivial analytical problem, even on a level of scaling relations [16]. For multicomponent vesicles [181], for instance, the effects of varying bending moduli and line tension between the components onto possible shape morphologies were studied for two liquid components [182], including some budding scenarios [183,184]. For more complex crystalline shells, the energetics of bilayer-formed polyhedral shapes was also studied [72,76]. The segregation of excess amphiphilic, intrinsically curved molecules in the regions of "energy focusing" (i.e., in ridges and vertices) as well as the formation of pores in the bilayer vesicles were suggested as possible scenarios of reduction of the total elastic energy of the shell. The elastic energy of various polyhedra with regular faces was enumerated for varying vesicle radii and fractions of a spontaneously curved component. Note, however, that the icosahedral shape does not always yield the absolute energy minimum [72,76] (see also Refs. [38,63,185]).

For two-component crystalline shells, which differ in several aspects from single-component ones, the ground-energy-state morphologies were analyzed, e.g., numerically by de la Cruz *et al.* [83,84,87]. The influence of a nonzero line tension between the components inhibiting the mixing of small domains and of the ratio of the bending moduli was examined. In particular, for small surface fractions of the soft phase (denoted by parameter f hereafter) and for low line tensions λ the material with low bending rigidities or "soft" material was shown to occupy the ridges of the icosahedron, while the rigid component was found to fill its faces. The energetic benefit from such stripelike edge-filling configurations was shown to diminish for smaller differences between the magnitudes of the elastic moduli of the two phases [83,84,87], as intuitively expected. This can trigger a phase separation or segregation of the two components on the shell surface at finite line tensions.

A rich phenomenology of various *nonicosahedral* shapes was shown to emerge as well, with a trend that the increasing line tension reduces the optimal number of soft domains emerging on the surface [83,84], as expected. The findings of our current model of soft-material "invasion" of a rigid crystalline shell (see Sec. III A) lead to similar conclusions. Importantly, the coarsening of rigid domains and subsequent phase separation was shown [83,84] to take place at the same critical $\lambda^\star$ value, irrespective of the soft-phase fraction f. The morphology of the equilibrium shapes of two-component fluid vesicles was also investigated [182,186].

Our objective here is to gain more insights into the physics and the energetics of the partitioning of a soft component on the crystalline two-component shell. We classify the "softness" of shell materials based on their FvK numbers (6) determined by the ratio of the respective stretching and bending moduli. Having in mind certain applications to icosahedral viruses, we only consider the outer protein layer of the capsids and model it as a thin shell. Indeed, the thickness of protein shells for a majority of viral capsids is $\sim 2 \ldots 5$ nm [74], that is much smaller than typical capsid dimensions. We neglect all features of compaction of nucleic acids (DNA and RNA) inside the capsid, as well as of possible interactions of nucleic acids with the inner capsid surface (involving, particularly for single-stranded RNA viruses, a significant electrostatically attractive component [25,33,48,65,69,80,187–194]). Some preliminary theoretical results for energetically optimal material partitionings on icosahedral two-component shells for a varying soft-component fraction f and interfacial line tension λ were presented recently [195].

Multicomponent viral shells and lipid vesicles have been examined from various viewpoints [83,84,95] and multiscale separation of lipids on multicomponent lipid vesicles due to lipid immiscibility or effective line tension between different phases were studied [196]. As an example of inhomogeneous shells, a spherical shell with a thinner and more elastic circular cap was shown by simulations [95] to require smaller external pressures to buckle and also yielding alternative postbuckling shell morphologies. In Ref. [95], however, no analytic calculations were presented for icosahedrally symmetric shells.

Let us also mention the experimental study of formation of hollow micron-sized icosahedral shells via segregation of oppositely charged surfactants [197,198] that has also motivated our research. The pores in the bilayer shell were shown to be formed particularly at the vertices of the icosahedron, reducing the elastic energy. The redistribution of the two types of surfactants on the surface was shown to optimize its total elastic and electrostatic energy. The excess molecules accumulate on the edges and pores of the capsid [197,198], avoiding the crystalline planar faces of the shell.

D. Plan of the paper and main concepts

The paper is organized as follows. In Sec. II A we start with the consideration of one-component crystalline shells (including icosahedral ones) and discussion of the basic model. We introduce the concepts of domes and cones in Sec. II B. The basic equations and their solutions for the strain energy are presented in Sec. II B 1, while variable cones are described in Sec. II C 1. We consider spherical domes rather than flat disks

to describe the buckling transition around a topological defect and compare the findings for the shell energetics with the known results [17,18] overviewed in Sec. I B. The energetics of the two-component shells, the main focus of this study, is examined in Sec. III where we show how the soft material progressively fills the spherical caps and invades the edges of the rigid crystalline shell to minimize the total elastic and line-tension energy. We start with the model description in Sec. III A, describe the stages of soft-material invasion and respective energy calculation in Sec. III B, and discuss the detail of stalling of the invasion process in Sec. III C. We show how the resulting level of invasion is stabilized against variations of the soft-material fraction. Finally, we summarize the main results in Sec. IV A and discuss some of their implications for the structure and stability of viral capsids in Sec. IV B.

II. SINGLE-COMPONENT SHELLS: RESULTS ON WRAPPING A CUTOUT DISK ONTO A DOME

We first discuss the approximations utilized in the model, consider the wrapping of a crystalline material onto a spherical cap, calculate the energy of an icosahedral shell composed of 12 domes, and compare the findings with the established results for buckled icosahedra [18].

A. Model and approximations

We consider a two-dimensional closed surface, with the area $4\pi R_{\rm shell}^2$ and the Euler characteristic $\chi_E = 2$, consisting of a crystalline material with underlying hexagonal symmetry. With a description of the shapes and energetics on the basis of planar-strain calculations and out-of-plane defect-buckling results, our findings provide, *inter alia*, a quantitative analytical description of the simulation data of Ref. [18]. We denote different energy contributions as E for the two-dimensional stretching, F for the bending, S for the line tension (in the case of two-component shells), and, finally, G for the total energy. As in similar studies [83], our energy-based treatment neglects fluctuations occurring at finite temperatures.

To compute the energetic cost of shell deformations, we employ the isotropic-elasticity theory of thin elastic sheets and the well known von Kármán equations (see Refs. [16,19,143]). We start with triangulated-lattice sheets which for biological systems mimic, e.g., densely packed lipids in membranes and regularly assembled capsomers in viral-capsid shells [9]. We improve the standard formulation for the disclination cones [18] by assuming a more realistic *spherical segment* for the cap, rather than a flat disk.

The "regularized" core of a conical disclination forms a spherical segment called "dome." This surface can (potentially) assume other functional geometries for optimizing the total elastic energy: one can determine the exact proportion and the extent of these "optimized surfaces" on the shell surface (e.g., as a function of the model parameters). For instance, the cap surface one can envisage a rotation surface of a catenary curve or of a parabolic arc. A functional optimization for the actual shape of nonspherical caps and of noncircular cylindrical segments can be a subject of future investigations. For simplicity, for both single- and two-component shells, we consider only perfectly spherical segments as domes (as rotation surfaces of circular arcs) and the cylindrical segments as the ridges connecting 12 spherical domes on an icosahedron. Spherical dome segments and smooth noncircular cones thus accommodate the disclination defects of a given charge, generalizing the simplistic picture of stretched flat caps (each containing a topological defect) and *nonsmoothly connected* bent circular cones, as initially proposed in Ref. [17].

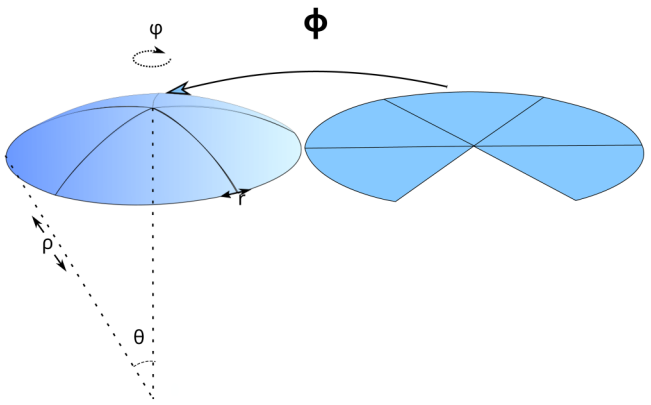

FIG. 2. Deformation map of a partial disk into a dome for the defect of charge $q = 1$. This corresponds to a cut-out planar azimuthal angle of $2\pi/6$, as for icosahedral shells. Some model parameters are denoted in the plot.

We evaluate the stretching and bending energies as a function of the size of spherical domes and FvK number. An important feature is that the critical *local* FvK number stays nearly constant at the boundary of the dome, thereby governing the cap-to-cone transition. Describing in-plane strain and out-of-plane buckling near the defects yields qualitative agreement with the simulation data [18]. The adjustment of parameters needed to be performed in Ref. [18] in order to make the agreement quantitative is attributed to the background curvature of the sphere. Note that continuum elastic theory is valid for large curvature radii, much larger than the shell thickness [16,19].

B. Modeling domes and cones

A *disclination* describes a rotational defect in the crystal structure. When going around a defect with the "topological charge" q on a triangulated lattice, the difference in directions of the respective vectors on the lattice is

$$q\pi/3. \tag{10}$$

To get an idea of how the strain develops along the dome, we set a mapping from a flat disk D_q with a $q\pi/3$ large wedge being cut out to a spherical dome of radius $\rho_{\rm dome}$ (see Fig. 2) (compare also to the disclination cone [19,136,137]). We compare configurations with

$$n_q = 12/q \tag{11}$$

defects for $q = \{1, 2, 3, 4\}$ assumed to be equally separated on the spherical surface (see Fig. 3) [199]. Each dome covers a solid angle $q\pi/3$ and its boundary is at the polar angle

$$\theta_{\rm dome} = \arccos[\bar{q}/6]. \tag{12}$$

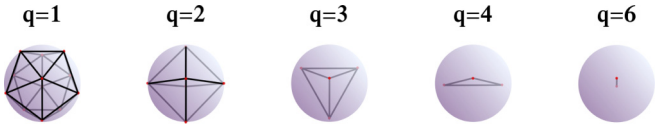

FIG. 3. Symmetric arrangements of topological defects of a given charge q on sphere that results in the energy minimum.

Here, the "dual" defect charge

$$\bar{q} = 6 - q \tag{13}$$

is equal to the coordination number of a given vertex [11].

We employ two key approximations. First, similarly to Ref. [18], we consider the wrapping to be rotationally symmetric around the vertical axis (see Fig. 2). This condition is violated stronger for larger domes and higher charge values q. When the radius of the dome gets small enough, the effects of neighboring defects are largely "screened" [14]. Second, the mapping does not change the area density. The exact deformation tensor, obtainable as a series expansion in the spherical harmonics (see, e.g., the approach of Ref. [18]), would show this, as a consequence of the harmonic properties of elastic forces. The deformation in a spherical dome does not preserve area density, but we take this as an approximation in order to obtain the relation between ρ_{dome} and r_{disk} (see below). This can also be seen in computer simulations [200] where the condition of constant area density holds over a large range of FvK numbers (up to the discretization size of the lattice). Locally this is not the case, but considering the remaining cone strainless makes it a consistent assumption. As a consequence, the relation between the radius of the disk (r_{disk}) and dome (ρ_{dome}) is given by

$$r_{\text{disk}} = \rho_{\text{dome}}\sqrt{2q/\bar{q}}, \tag{14}$$

where ρ_{dome} is the radius of a sphere yielding the spherical dome as a segment [201].

1. Strain energy

The mapping onto the dome surface is given by spherical angles (polar angle θ and azimuthal angle ϕ) as functions $\phi(r, \psi)$ and $\theta(r, \psi)$ in the polar coordinates on the disk r and ψ, that is,

$$\phi(\psi) = (6/\bar{q})\psi \tag{15}$$

and

$$\theta(r) = \arccos\left(1 - \frac{\bar{q}}{12}\frac{r^2}{{\rho_{\text{dome}}}^2}\right). \tag{16}$$

The *deformation tensor* $\bar{\boldsymbol{\gamma}}$ has the diagonal structure due to the symmetry present. It is defined as half the difference between the metric on the disk and dome, with the r and ψ components being, respectively,

$$\bar{\gamma}_{rr}(u) = -\frac{4q^2 - \bar{q}u^2}{48 - 2\bar{q}u^2} \quad \text{and} \quad \bar{\gamma}_{\psi\psi}(u) = \frac{q}{2\bar{q}} - \frac{u^2}{8}, \tag{17}$$

where

$$u = r/\rho_{\text{dome}} \tag{18}$$

is the dimensionless radial variable. Generally, $\rho_{\text{dome}} \leqslant R_{\text{shell}}$ and they are equal at $\gamma \leqslant \gamma_b$. Above buckling, the value of ρ_{dome} is found by minimizing the total energy (namely, of the strain in the dome and the bending energy in the cone).

The bending energy of the dome is a constant independent of ρ_{dome}. In fact, changing the values of K or κ changes ρ_{dome} such that the FvK number (6) is equal to its buckling value. The strain energy in the dome surface for

$$u \leqslant u_{\text{disk}} = r_{\text{disk}}/\rho_{\text{dome}} \tag{19}$$

follows from the general elasticity theory in the limit of small deformations [16,18,19,202]

$$E_{\text{dome}}(u) = \frac{K{\rho_{\text{dome}}}^2 \int_0^u du' \int_0^{\frac{\bar{q}}{3}\pi} d\psi [\text{Tr}(\bar{\boldsymbol{\gamma}}(u')^2) + 2\sigma \text{Det}(\bar{\boldsymbol{\gamma}}(u'))]}{2(1-\sigma^2)}, \tag{20}$$

where K is the two-dimensional Young modulus and σ is the two-dimensional Poisson ratio of the material. Here $\text{Tr}(\dots)$ and $\text{Det}(\dots)$ are the trace and the determinant of a matrix, respectively. Note that the factor $\bar{q}\pi/3$ emerges from the surface integral in Eq. (20). Then, via inserting expression (17) into Eq. (20), fixing the Poisson ratio to

$$\sigma = 1/3 \tag{21}$$

(the value for the regular triangular lattice that is also a realistic number for many viral-capsid shells [39,43,46]), and performing the integration, the elastic energy of the dome in terms of u becomes

$$E_{\text{dome}}(u) = \frac{\pi K {\rho_{\text{dome}}}^2}{128}\left[\frac{2\bar{q}^3u^2}{24-\bar{q}u^2} + 10\bar{q}u^2 + \frac{(24-\bar{q}u^2)^2}{\bar{q}} - \frac{(24-\bar{q}u^2)^3}{16\bar{q}^2} - \frac{288(9-2q)}{\bar{q}^2} + 32\bar{q}\log\left(1-\frac{\bar{q}}{24}u^2\right)\right]. \tag{22}$$

This general expression improves the classical description of the strain of a flat disk [Eq. (4)] [17]. The strain energy of a dome increases sharply with the defect charge q (see Table I). However, when the energy magnitude and the parameter u are scaled with their respective maximal values, the strain energy becomes approximately quadratic in variable

$$u/u_{\text{dome}} = r/r_{\text{disk}}, \tag{23}$$

with

$$u_{\text{dome}} = \sqrt{2q/\bar{q}}, \tag{24}$$

so that we use the ansatz

$$E_{\text{dome}}(u) \simeq E_{\text{dome}}\left(\sqrt{\frac{2q}{\bar{q}}}\right)\frac{\bar{q}}{2q}u^2 = K\frac{qA_q}{12}{\rho_{\text{dome}}}^2\left(\frac{u}{u_{\text{dome}}}\right)^2, \tag{25}$$

TABLE I. Strain energies of the shell (in units $KR_{\rm shell}^2$) for varying defect charges q (see Fig. 3) computed from Eq. (26) and the Green's function calculations outlined in Sec. II B 2.

	$q=1$	$q=2$	$q=3$	$q=4$	$q=6$
	Icosahedron	Octahedron	Tetrahedron	Triangle	Line
A_q	0.04819	0.2670	0.9702	3.685	Not defined
$\frac{E_{\rm shell}}{KR_{\rm shell}^2}$	0.05273	0.2184	0.5147	1.0281	2.2310

where the coefficient A_q is

$$A_q = 3\pi\frac{\bar{q}}{q}\left[q\frac{4q^4-129q^3+1536q^2-7488q+13824}{64(12-q)\bar{q}^3} + \log\left(1-\frac{q}{12}\right)\right]. \tag{26}$$

This expression for A_q is obtained from Eq. (22) after setting $u = u_{\rm dome}$.

The quadratic approximation (25) is equal to the full solution (22) at the end points (see Fig. 4). The magnitude of A_q, obtained from the Green's function calculations of Ref. [14] (see Sec. II B 2), as listed in Table I, agree favorably with the exact results [14] for $q = 1$. The agreement, however, becomes less favorable as the defect charge increases. The curves for the strain energy of the dome for all q values as a function of $r/r_{\rm disk}$ collapse onto the *universal* curve (see Fig. 4). The approximate quadratic dependence obtained from Eqs. (22) and (25) is the dashed curve in Fig. 4. In virtue of Eqs. (23) and (25), the strain energy of the dome is also a quadratic function of the radius r of a flat disk, namely,

$$E_{\rm dome}(r) \simeq K\frac{qA_q}{12}{\rho_{\rm dome}}^2\frac{r^2}{r_{\rm disk}^2}. \tag{27}$$

For a single defect, we find that for smaller sphere radii the area over which the crystalline material relaxes its strain also becomes smaller. This tendency of *Gaussian-curvature focusing* is counterbalanced by the bending energy, for which the sphere is energetically optimal. This competition regulates the buckling propensity of surfaces and controls their minimal-energy shapes.

Then, with Eq. (26), the strain energy of the entire sphere covered with $12/q$ domes becomes

$$E_{\rm shell} = KA_qR_{\rm shell}^2. \tag{28}$$

Although the general result (20) depends on the Poisson ratio, when $\sigma = \frac{1}{3}$ for a regular triangular lattice [58,83,84,94,203] is used, they become quite close to those reported in Ref. [14]. Equations (22), (25), and (26) are the main results of this section.

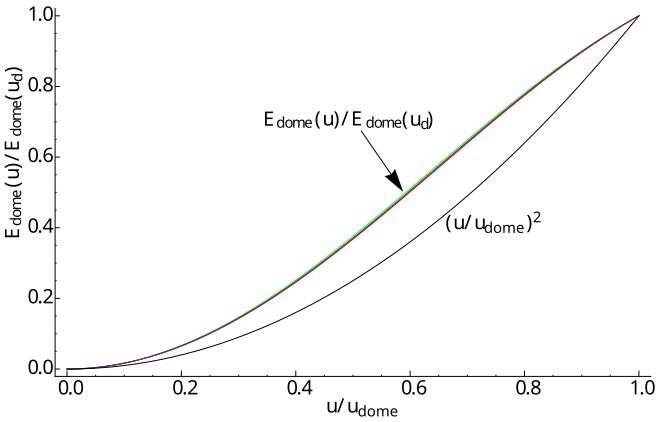

FIG. 4. Scaled in-plane strain energies of the dome given by Eq. (22) computed for $q = \{1, 2, 3, 4, 6\}$ (almost fully superimposing curves of different colors), collapse onto a single universal curve. The values of A_q from Table I were used here. The quadratic law for the bottom curve is Eq. (25), illustrating a rather close agreement with the exact result (22).

2. Green's function approach

Following Ref. [14], for an arbitrary arrangement of n defects on a closed surface we can write

$$E_{\rm shell} = \frac{K}{2}\oint_S d\mathbf{x}^2\oint_S d\mathbf{y}^2[K_{\rm G}(\mathbf{x})-q(\mathbf{x})]\triangle^{-2}(\mathbf{x},\mathbf{y}) \times[K_{\rm G}(\mathbf{y})-q(\mathbf{y})]+E_{\rm core}. \tag{29}$$

We choose one defect positioned on the sphere's "north pole," while the coordinates for other defects are computed in Table II. Here, $K_{\rm G}(x)$ is the Gaussian curvature at point x, $q(x)$ is the topological charge (that is effectively a sum of delta functions), and the operator $\triangle^{-2}$ is the inverse of the Laplacian square. $E_{\rm core}$ is the short-distance core energy that depends on the details of intermolecular interactions in the shell material at the "microscopic" level [204] We tabulate $E_{\rm shell}$ in Table I without including the results for $E_{\rm core}$.

3. Bending energy

The bending energy depends only on the solid angle each dome covers on the shell. With the mean curvature of the dome,

$$H_{\rm dome} = 1/\rho_{\rm dome}, \tag{30}$$

the contribution to the elastic energy amounts to

$$F_{\rm dome} = 2\kappa H_{\rm dome}^2(q\pi/3){\rho_{\rm dome}}^2 = \kappa 2q\pi/3. \tag{31}$$

The details of the Gaussian-curvature contribution will be omitted below, except for pursuing a comparison with computer simulations [18], as the saddle-splay modulus is often not known (because it depends on the molecular details of the material). Next, we treat the cone that starts strainless at the radius $r = r_{\rm disk}$. The strainless cone has the radius

$$\rho_{\rm cone}(r) = (6/\bar{q})r \tag{32}$$

TABLE II. Coordinates θ and ϕ of defect positions on symmetric solids, computed for integer defect charges.

Symmetry	Defects	$\cos\theta$	ϕ				
Icosahedron	$12 \times q = 1$	1			Indefinite		
		$\frac{1}{\sqrt{5}}$	$\frac{4\pi}{5}$	$\frac{2\pi}{5}$	0	$-\frac{2\pi}{5}$	$-\frac{4\pi}{5}$
		$-\frac{1}{\sqrt{5}}$	$\frac{\pi}{5}$	$\frac{3\pi}{5}$	π	$-\frac{3\pi}{5}$	$-\frac{\pi}{5}$
		-1			Indefinite		
Octahedron	$6 \times q = 2$	1			Indefinite		
		0	0	$\frac{\pi}{2}$	π	$\frac{3\pi}{2}$	
		-1			Indefinite		
Tetrahedron	$4 \times q = 3$	1			Indefinite		
		$-1/3$	0	$\frac{\pi}{3}$	$\frac{2\pi}{3}$		
Double triangle	$3 \times q = 4$	1			Indefinite		
		$-\frac{1}{3}$	0	$\frac{\pi}{3}$	$\frac{2\pi}{3}$		
Cylinder	$2 \times q = 6$	± 1			Indefinite		
Plane	$1 \times q = 12$	1			Indefinite		

and height

$$z_{\text{cone}}(r) = -\sqrt{q(12-q)}r/6, \tag{33}$$

as functions of distance r. The mean curvature of the dome then becomes

$$H_{\text{dome}} = \frac{\sqrt{q(12-q)}}{2\bar{q}r}. \tag{34}$$

Note that the principal radius of curvature of the cone $1/k_{\text{cone}}$ at the value r_{disk} is, in fact, smaller than ρ_{dome},

$$\frac{1}{k_{\text{cone}}} = \sqrt{\frac{2\bar{q}}{12-q}}\rho_{\text{dome}}. \tag{35}$$

The bending energy of the cone features a *logarithmic* dependence on the shell radius [16,19]

$$F_{\text{cone}}(R_{\text{shell}}) = \kappa\frac{qB_q}{12}\log\left(\frac{R_{\text{shell}}}{\rho_{\text{dome}}}\right) \propto \log(R_{\text{shell}}), \tag{36}$$

with the coefficient

$$B_q = 2\pi(12-q)/\bar{q}. \tag{37}$$

To check the accuracy of the dome-related part of the energy of this model, we compare the icosahedral positioning of $q = 1$ defects with the exact results [14] that yields for 12 defects the shell energy

$$E_{\text{shell}} \approx 0.05273 \times KR_{\text{shell}}^2. \tag{38}$$

Comparing this with the stretching energy of 12 domes given by Eq. (28) having the same radius, we get $A_1 \approx 0.04819$ in Eq. (26), that is <10% away from the exact result [14]. For the symmetric arrangement of defects of higher charges, $q = \{2, 3, 4, 6\}$ as in Fig. 3, the calculations go along the lines of Ref. [14] and their findings are presented in Table I. For higher q values, the agreement of our model with the exact results [14] is less satisfactory.

4. Cone buckling

In Ref. [18] a remarkably good agreement of the results of computer simulations for the elastic energy of shells and of findings of a simple theoretical model of elasticity was obtained. A defect on spherical surface was treated as a defect on a flat surface that buckles into a strainless cone (the results were computed using some approaches for two-dimensional crystals [17]). The adjustment of parameters in Ref. [18] needed for this agreement was attributed to the background curvature of the sphere. In our current approach, the elastic energy of the cone is the same and, as we adjust the coefficient in the elastic energy of the dome [see Eq. (25)], our results are not expected to fit the data better than the original [18] flat-cap shell-buckling approach.

Following Ref. [18], we minimize the total energy of the domes and cones, given by Eqs. (25), (26), and (36), with respect to the dome radius. This results in a critical FvK number above which buckling takes place,

$$\gamma_b = B_q/(2A_q). \tag{39}$$

The elastic energy of the entire shell with $12/q$ defects is then given by [16,18]

$$\frac{G_{\text{shell,cone}}(\gamma)}{\kappa} = \begin{cases} A_q\gamma + 8\pi/3, & \gamma \leqslant \gamma_b \\ B_q[1+\log(\gamma/\gamma_b)]/2 + 8\pi/3, & \gamma > \gamma_b. \end{cases} \tag{40}$$

In this expression, similarly to Ref. [18], we added the constant energy term $8\pi/3$ corresponding to the Gaussian-curvature contribution for a harmonic triangular lattice, to achieve a better comparison with the results of computer simulations [18]. As shown in Fig. 5, there is a notable mismatch between the theoretical results and simulations. It also shows a discrepancy between the results of simulations [18] and the Green' s function calculations of Ref. [14].

Therefore, we perform below the "adjustment" of the elastic moduli to reach a better agreement with simulations of Ref. [18]. We first adjust the value of K as $K \to 1.2K$ or, equivalently,

$$\gamma \to 1.2\gamma, \tag{41}$$

in virtue of Eq. (6). This adjustment follows from the least-square fit of the shell-energy data [18] for FvK numbers in the range $\gamma \leqslant 110$. Physically, a finite mesh size used in simulations [18] gives rise to the empirical factor 1.2, compared to the respective moduli in the continuous elasticity

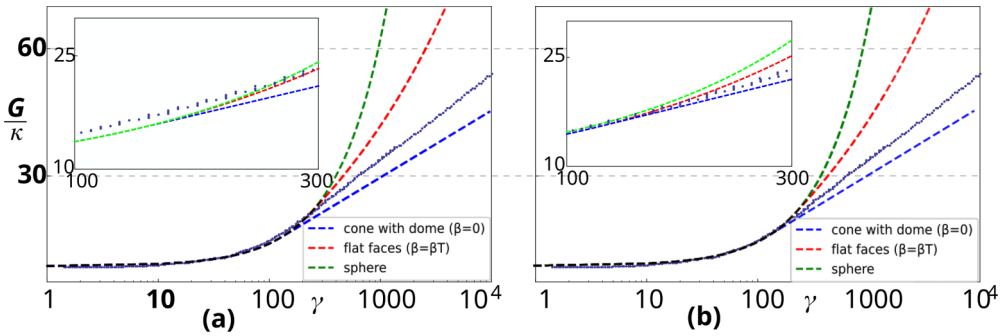

FIG. 5. Normalized total elastic energy of a closed crystalline surface as a function of the FvK number γ before (a) and after (b) the finite-mesh adjustment of parameters, given by Eqs. (42) and (44). Both the main plots and insets are in log-linear scale. The dotted dark blue curves show the results of computer simulations performed in Ref. [18]. The bending and strain energy of the sphere is the dashed green curve (see the legend). The energy of the cylindrical segments at $\beta_{\rm cyls} \to \beta_T$, when the faces of the shell are flat, is the dashed red curve, calculated from Eq. (67) upon minimization with respect to $x_{\rm dome}$ (it contains also the strain in the domes and all bending contributions). The results of the approach of circular cones and spherical domes are shown as the dashed light blue curves. The insets show the crossing of the energy curves occurring at moderate γ values.

theory. Following Ref. [18] and comparing theoretical results versus computer-simulations data [18] in the region $\gamma \leqslant 10^4$ we adjust B_q value to

$$B_q^{\rm adj} = 1.2 B_q, \tag{42}$$

and the critical buckling number becomes

$$\gamma_b \simeq 134, \tag{43}$$

like in Ref. [18]. For the further analysis we use

$$A_q^{\rm adj} = 1.2 A_q. \tag{44}$$

When we let buckling start with cylindrical segments and flat faces, that corresponds to $\beta = \beta_T$ given by Eq. (45), the buckling γ decreases to $\gamma_b = 121$ [see Eq. (74)]. The energy deviations from the analytical cone-dome approach remain, however, still substantial [Fig. 5(b)]. One viable reason is geometric "frustrations" occurring upon inevitably *nonsmooth* "gluing together" of $12/q$ defect-centered dome-plus-cone parts into a full shell. The length of the cylindrical segments in this model is set to minimize the combined strain of the spherical segments with the bending energy of the cylindrical segments, while the bending energy of the domes stays constant. In Sec. II C, we geometrically describe the actual shape of the domes just prior to buckling.

C. Cone morphing

Here, we present more accurate energy calculations of the buckling transition in rigid-crystalline single-component cones and domes, as compared to Ref. [18]. We first consider the energetics of the edges connecting the 12 domes on the shell surface, and then develop a *variable-cone* approach that enables us to consider a *secondary buckling transition*, with noncircular cone shapes optimizing the shell energy (see Fig. 6). Below, we introduce a family of models interpolating between the cone model and the model of cylindrical segments as edges. We envisage the formation of cones at the buckling transition as the breaking up of the sphere into $12/q$ domes. The natural way of doing so is to divide the sphere into the spherical domes, shrink the domes, and then connect them with strainless cylindrical segments and flat faces.

1. Variable-cone approach: Geometry

The motivation for this extension of the model of circular cones to noncircular cross sections is twofold. First, we aim at a better understanding of possible noncircular cone shapes for the conditions of increasing rigidity of the shell material. Second, it is to examine the conditions favoring the filling of ridges with the soft material in the model of two-component shells (see Sec. III A below). From the perspective of virus capsids, this modification of the shell-buckling theory is motivated by a remarkable "stargate" formation of protein subunits on the capsids of giant mimivirus [40] (see also Sec. IV B). The arguments below are in some aspects similar to those proposed for the secondary shell-buckling transition in Ref. [140].

We still assume all strain to be concentrated in a "generalized dome" centered around the defect. We construct a family of variable cones with the shapes ranging from edges with flat faces in-between them to circular-cone shapes (see the examples illustrated in Fig. 6). Since we treat each of $12/q$ parts of the spherical dome separately, we name the tubular parts of the edges as "cylindrical segments" and denote them by the index "cyls" below. Due to the shell symmetry, such a cylindrical segment has half the length of a respective edge. The face area in-between the two neighboring cylindrical segments and the cone base is called below the variable cone denoted by the index "v cone." One face of the icosahedron consists of three faces of such v cones. The variable-cone model "interpolates" between the models of circular cones and of cylindrical segments as edges of the shell.

We treat the geometry for a defect charge $q = 1, \ldots, 4$ and consider a configuration with $\bar{q} = 6 - q$ cylindrical segments of radius $\rho_{\rm cyls}$ covering a tubular or central angle $2\beta_{\rm cyls}$ which connect a given dome with its neighbors on the shell. This angle describes the amount of cone curvature transferred to the edges: the maximal value of $\beta_{\rm cyls}$ is given by the

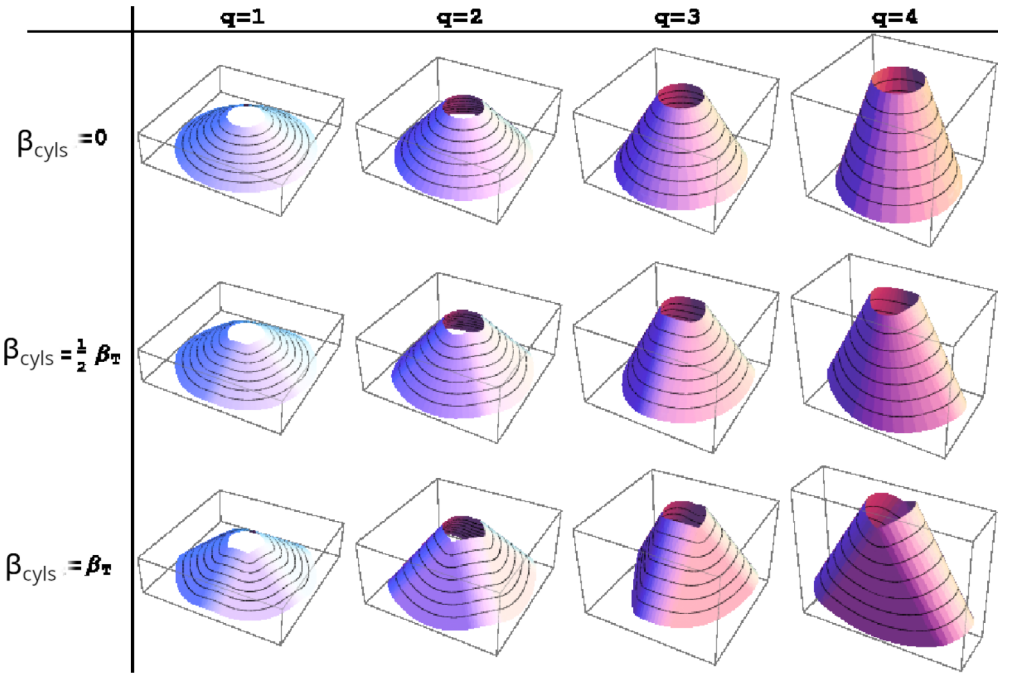

FIG. 6. Variable cones of noncircular cross section: cylindrical segments with the cone surfaces visualized for $q = \{1, 2, 3, 4\}$ defining the cylindrical segment angle (see Sec. II C 1 for details). The first row are the standard or pure cones, the structures in the middle row contain half-formed cylindrical segments , while the structures in the last row are partial cylindrical segments with flat faces between them. The length of the boundary remains the same in all panels. The empty spaces left on top of the cones are to be filled in the model with the corresponding domes.

geometry as

$$\beta_T(q) = \arccos\left[\frac{\cos(\pi/\bar{q})}{\cos(\pi/6)}\right]. \tag{45}$$

At $\beta_{\text{cyls}} = \beta_T(q)$ the remaining surface of the variable cones is flat (see the dashed red curves in Fig. 5).

We use the notation $R_i(\phi)$ for rotation matrices with angle ϕ around the unit vector $\vec{e}_i$ pointing in direction of the positive i axes, where $i \in \{x, y, z\}$. A possible parametrization for the nth cylindrical segment is

$$\mathbf{cyls}_n(y, \beta) = R_z\left(\frac{2n\pi - \pi}{\bar{q}}\right) R_x(-\alpha) R_y(\beta) \begin{pmatrix} 0 \\ y \\ \rho_{\text{cyls}} \end{pmatrix}, \tag{46}$$

where α is an angle (still to be determined) of the cylindrical segment with the tangent plane to the dome top, as detailed in Fig. 7. Here, the index n varies from 0 to $(\bar{q} - 1)$ and represents $\bar{q}$ cylindrical segments (not to be confused with n_q),

$$\beta \in \{-\beta_{\text{cyls}}, \beta_{\text{cyls}}\} \tag{47}$$

is the cental angle, and y is the coordinate along the cylindrical segment (see Fig. 7). The dot in Eq. (46) and below denotes matrix multiplication and $\mathbf{cyls}_n$ stands for the cylindrical segment with angle β denoting a rotation angle around the cylinder axis [205]. We assume that the strain in the cylindrical segments and variable cones can be neglected. We thus set

$$y = r + C, \tag{48}$$

with r being the material distance to the defect [or the radial coordinate in the (r, ψ) plane] and C is a constant. The latter is used to translate the cylindrical segment along its axis to make its start fit with the spherical segment.

Let

$$\vec{t}_n(\beta) = R_z\left(\frac{2n\pi - \pi}{\bar{q}}\right) R_x(-\alpha) R_y(\beta) \cdot \vec{e}_x \tag{49}$$

be the tangent to the nth cylindrical segment normal to its axis. We construct the variable cone between $\mathbf{cyls}_n$ and $\mathbf{cyls}_{n+1}$ by connecting the points $\mathbf{cyls}_n(y, -\beta_{\text{cyls}})$ and $\mathbf{cyls}_{n+1}(y, \beta_{\text{cyls}})$ with a circular arc that connects differentiably smoothly with the cylindrical segment arcs at $y(r)$ [206]. We parametrize the constructed arc of the v cone with r-dependent radius ρ_{face} and angle ϕ varying in the range

$$\phi \in \{-\phi_{\text{face}}, \phi_{\text{face}}\}. \tag{50}$$

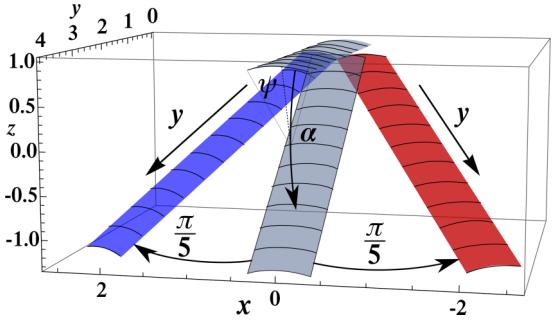

FIG. 7. Construction of the $n = 0$ (blue) and $n = 1$ (red) cylindrical segments for $q = 1$ defect with the maximal tubular angle. The slope angle $\alpha(q = 1)$ is given by $\arccos[\sin(\pi/6)/\sin(\pi/5)]$.

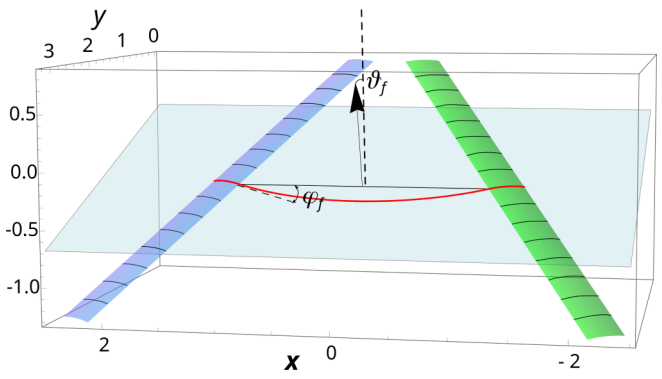

FIG. 8. Two cylindrical segments forming the edges of a variable cone. The blue inclined plane contains the bases of the arcs tilted by an angle θ_{face}. The face angle θ_{face} is denoted as well [see Eq. (56) for details].

We construct the variable cone between the $n = 0$ and 1 cylindrical segment in Fig. 8. The approach with a continuous first derivative at this connection of a cylindrical segment and a dome (meaning a continuous tangent plane) yields the condition

$$\begin{aligned}\cos(\phi_{\text{face}}) &= \vec{t}_0(-\beta_{\text{cyls}}) \cdot \vec{e}_x \\ &= \cos(\pi/\bar{q})\cos(\beta_{\text{cyls}}) \\ &\quad + \sin(\pi/\bar{q})\sin(\alpha)\sin(\beta_{\text{cyls}}). \end{aligned} \tag{51}$$

The distance between the two boundary points gives the constraint

$$\begin{aligned}2\rho_{\text{face}}\sin(\phi_{\text{face}}) &= |\mathbf{cyls}_0(y, \beta_{\text{cyls}}) - \mathbf{cyls}_1(y, -\beta_{\text{cyls}})| \\ &= 2y\ \sin(\pi/\bar{q})\cos(\alpha) \\ &\quad + 2\rho_{\text{dome}}[\sin(\pi/\bar{q})\sin(\alpha)\cos(\beta_{\text{cyls}}) \\ &\quad - \cos(\pi/\bar{q})\sin(\beta_{\text{cyls}})]. \end{aligned} \tag{52}$$

With no strain in the variable cones, the arc length is

$$2\rho_{\text{face}}\phi_{\text{face}} = \pi r/3 - 2\beta_{\text{cyls}}\rho_{\text{cyls}}. \tag{53}$$

Combining Eqs. (52) and (53) we obtain

$$\begin{aligned}&\frac{\sin(\phi_{\text{face}})}{\phi_{\text{face}}}\frac{\pi}{6}r - \frac{\sin(\phi_{\text{face}})}{\phi_{\text{face}}}\beta_{\text{cyls}}\rho_{\text{cyls}} \\ &= (r + C)\sin(\pi/\bar{q})\cos(\alpha) \\ &\quad + \rho_{\text{cyls}}[\sin(\pi/\bar{q})\sin(\alpha)\cos(\beta_{\text{cyls}}) \\ &\quad - \cos(\pi/\bar{q})\sin(\beta_{\text{cyls}})]. \end{aligned} \tag{54}$$

As r varies continuously, requiring a constant variable-cone angle ϕ_{face} results in the relation

$$\frac{\sin(\phi_{\text{face}})}{\phi_{\text{face}}}\frac{\pi}{6} = \sin(\pi/\bar{q})\cos(\alpha), \tag{55}$$

that combined with Eq. (51) gives α and ϕ_{face} as well as after using (53) also yields ρ_{face}.

The parametrization is completed with the angle θ_{face}, the normal of the plane containing the variable-cone arc makes with the z axis,

$$\cos(\theta_{\text{face}}) = \frac{\vec{t}_0(-\beta_{\text{cyls}}) \wedge \vec{e}_x}{|\vec{t}_0(-\beta_{\text{cyls}}) \wedge \vec{e}_x|}. \tag{56}$$

Here $\vec{e}_x \wedge \vec{e}_y$ denotes a two-form, that is the cross-product of two one-forms that are defined in the cotangent space of a manifold (for a two-dimensional manifold this yields a volume form).

The area two-form and the mean curvature of the variable cone are

$$\omega_{\text{face}} = \frac{\pi r - 6\rho_{\text{cyls}}\beta_{\text{cyls}}}{6\phi_{\text{face}}}(dr \wedge d\phi) \tag{57}$$

and

$$H_{\text{face}} = \frac{\pi\sqrt{(6\phi_{\text{face}}/\pi)^2 - 1}}{2(\pi r - 6\rho_{\text{cyls}}\beta_{\text{cyls}})}, \tag{58}$$

respectively. In Eq. (56), $\vec{e}_x$ is a unit vector in the x direction and the wedge product is the normal cross-product of the two vectors. In Eq. (57) the area (volume two-form) is written as a wedge product between the one-forms: as their two-dimensional surface is imbedded in three dimensions it is effectively also a cross-product of vectors in the r and ϕ directions.

The resulting surfaces for different defect charges are depicted in Fig. 6. The variable cones and the cylindrical segments are Gaussian flat. We set the radius r_{disk} to the sum of the arc lengths of the maximal cylindrical segments,

$$r_{\text{disk}}^{\max} = 6\beta_T(q)\rho_{\text{cyls}}/\pi, \tag{59}$$

that yields

$$\rho_{\text{cyls}} = \frac{\pi}{6\beta_T(q)}\sqrt{\frac{2q}{\bar{q}}}\rho_{\text{dome}}. \tag{60}$$

From Eq. (57) we find that r runs from ρ_{dome} to $\sqrt{2q/\bar{q}}R_{\text{shell}}$, independent on β_{cyls}.

2. *Variable-cone approach: Energy calculation*

The bending energies of the variable cone and cylindrical segment are, respectively,

$$\begin{aligned}F_{\text{v cone}} &= 2\kappa\iint_{\text{face}}\omega_{\text{face}}H_{\text{face}}^2 \\ &= \kappa\frac{\pi}{6}\left[\left(\frac{6\phi_{\text{face}}}{\pi}\right)^2 - 1\right]\log\left[\frac{1 - \beta_{\text{rel}}x_{\text{dome}}}{(1 - \beta_{\text{rel}})x_{\text{dome}}}\right], \end{aligned} \tag{61}$$

and

$$F_{\text{cyls}} = \kappa\frac{6\beta_T^2\beta_{\text{rel}}}{\pi}\left(\frac{1}{x_{\text{dome}}} - 1\right). \tag{62}$$

Here, we denoted

$$x_{\text{dome}} = \rho_{\text{dome}}/R_{\text{shell}} \tag{63}$$

and the relative or *normalized* cylindrical segment angle (denoted by the index "rel" below)

$$\beta_{\text{rel}} = \beta_{\text{cyls}}/\beta_T(q), \tag{64}$$

takes values from zero to one. The relative dome radius x_{dome} for a given value of β_{rel} is determined via energy minimization.

Expression (61) can be simplified by noting that the square-root factor from Eq. (58) is nearly linear in β_{rel}, as we demonstrate in Fig. 9. At this point, we cannot provide a

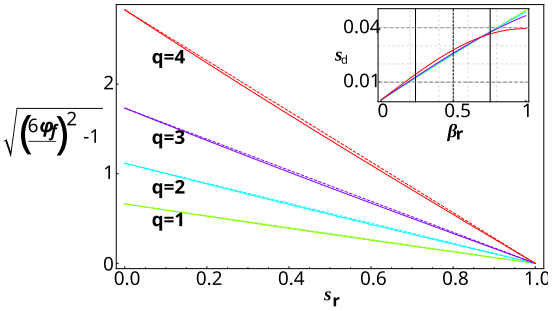

FIG. 9. The square-root factor from the mean curvature for the variable cone, Eq. (58), with a linear fit computed as function of parameter $\beta_{\rm rel}$ given in (64), shown for several values of the defect charge q. The inset shows the standard deviation denoted as s_d from the linear fit.

simple physical meaning for this linearity. As for $\beta_{\rm rel} = 0$ we have $\phi_{\rm face} = \pi/\bar{q}$, the bending energy of the variable cone takes a rather simple form

$$F_{\rm v\ cone} = \kappa \frac{q B_q^{\rm adj}(1-\beta_{\rm rel})^2}{12\bar{q}} \log\left[\frac{1-\beta_{\rm rel} x_{\rm dome}}{(1-\beta_{\rm rel})x_{\rm dome}}\right]. \quad (65)$$

We thus have, in fact, a simple interpolation between the models of the cone and of the cylindrical segments with the flat shell faces.

Adding all these ingredients together, the energy of the entire shell composed of $12/q$ variable cones is (with the usual $8\pi/3$ term being added)

$$\frac{G_{\rm shell,v\ cone}}{\kappa} = A_q^{\rm adj}\gamma + \frac{8\pi}{3}, \quad \gamma \leqslant \gamma_{b,\rm v\ cone} \quad (66)$$

and

$$\frac{G_{\rm shell,v\ cone}}{\kappa} = \gamma x_{\rm dome}^2 A_q^{\rm adj} + (1-\beta_{\rm rel})^2 B_q^{\rm adj} \log\left[\frac{1-\beta_{\rm rel}x_{\rm dome}}{(1-\beta_{\rm rel})x_{\rm dome}}\right] + \frac{72\bar{q}\beta_T^2}{\pi q}\beta_{\rm rel}\left(\frac{1}{x_{\rm dome}} - 1\right) + \frac{8\pi}{3}, \quad \gamma > \gamma_{b,\rm v\ cone}. \quad (67)$$

The buckling takes place at the FvK number

$$\gamma = \gamma_{b,\rm v\ cone} = (1-\beta_{\rm rel})\frac{B_q^{\rm adj}}{2A_q^{\rm adj}} + \frac{36\bar{q}\beta_T^2(q)}{\pi q A_q^{\rm adj}}\beta_{\rm rel}, \quad (68)$$

as follows from Eq. (66). Buckling occurs when the value of $x_{\rm dome} \in [0, 1]$ that minimizes $G_{\rm shell,v\ cone}$ in Eq. (67) is equal to unity. One can also show that for $\gamma < \gamma_{b,\rm v\ cone}$ the physically impossible situation may emerge, for which $x_{\rm dome} > 1$, so $x_{\rm dome}$ keeps the maximal value of unity, and then Eq. (67) turns into Eq. (66).

The resulting energy curves are presented in Fig. 10, evaluated for several $\beta_{\rm rel}$ values. We find that for each range of FvK numbers, up to a given γ value, there exists an *optimal angle* of the cylindrical segments $\beta_{\rm rel}$ that gives the closest agreement for the $G_{\rm shell,v\ cone}/\kappa$ versus γ curve with the results of computer simulations of Ref. [18] in this range. Typically, the higher the FvK number is, the smaller is the

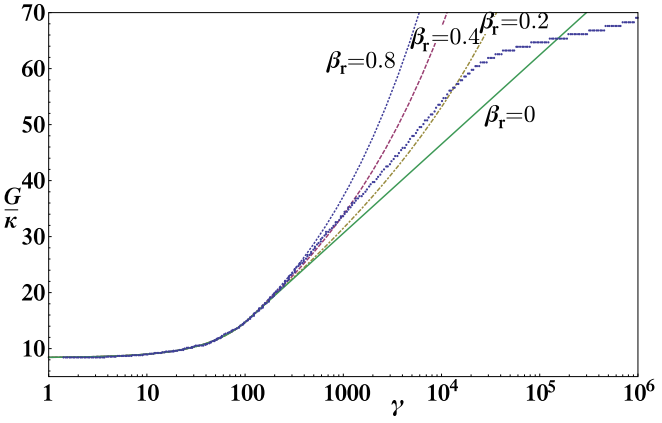

FIG. 10. Energy curves for variable cones computed for several $\beta_{\rm rel}$ values using Eq. (66) shown with the simulation data of Lidmar *et al.* [18] (the blue dots).

optimal cylindrical segment angle predicted by this model. This is an interesting fact *contradicting* the usual picture of buckling [18] that implies that one starts with a cone and ends up in the high-γ limit with cylindrical segments of a vanishing radius which connect the nearly flat faces of the shell. The current energy-optimized picture of v cones is quite different. Namely, the cylindrical segments slowly evolve into the variable cones with increasing γ values, until the cylindrical segments disappear at larger FvK numbers, at the energy plateau shown in Fig. 10.

At much higher FvK numbers, in the range $\gamma \gtrsim 10^6$ (see Ref. [18]), the Witten *et al.* regime [126,132] for the ridge energy can have a dominant contribution, with the scaling relation for progressively sharpening ridges (in the continuum limit) being

$$G_{\rm shell,ridge}(\gamma) \sim \gamma^{1/6}. \quad (69)$$

Note, however, that the plateaulike energy behavior observed in simulations [18] at large FvK numbers is a possible effect of a finite mesh size [207].

The functional dependencies of $\beta_{\rm rel}$ and $x_{\rm dome}$ on γ are shown in log-log scale in Fig. 11. Surprisingly, we observe a power-law decrease of $\beta_{\rm rel}(\gamma)$ over a wide range of FvK numbers, namely,

$$\beta_{\rm rel}(\gamma) \sim \gamma^{-0.5}. \quad (70)$$

The scatter of $\beta_{\rm rel}(\gamma)$ at small γ values in Fig. 11 is a consequence of convergence of all curves when approaching γ_b:

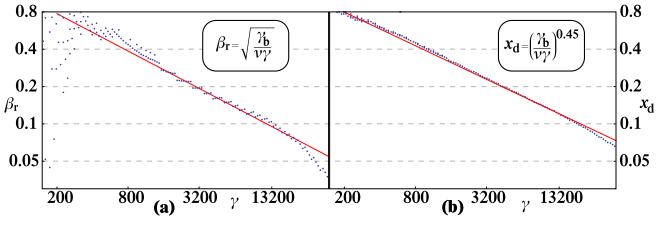

FIG. 11. Scaling of the parameters $\beta_{\rm rel}$ (a) and $x_{\rm dome}$ (b) with the FvK number. The red solid lines are the asymptotes (70) and (71), while the data points are the results of Ref. [18].

in this regime a small change in γ can lead to a large change in $\beta_{\rm rel}$. The drop of $\beta_{\rm rel}(\gamma)$ observed after $\gamma \simeq 10^4$ is the start of the energy plateau, also visible at large FvK numbers in Fig. 10. Within the model of v cones, the angle $\beta_{\rm cyls}$ gets smaller with increasing γ, but does not reach zero before the energy "plateau." For the $x_{\rm dome}(\gamma)$ dependence a similar power-law decay is also observed, with a close value of the exponent,

$$x_{\rm dome}(\gamma) \sim \gamma^{-0.45}. \tag{71}$$

The existence of scalings (70) and (71) is somewhat surprising per se. One may speculate on precise physical reasons of a small difference in the exponent values [208]. This difference may reflect imperfections of the current model (this subject deserves future investigation).

For the further analysis, we use the simplification

$$\beta_{\rm rel} = x_{\rm dome} = \sqrt{\frac{\gamma_{b,\text{v cone}}(\beta_{\rm rel}=1)}{\gamma}}, \tag{72}$$

resulting in a critical FvK number for buckling,

$$\gamma_{b,\text{v cone}} = \frac{36\bar{q}\beta_T^2(q)}{\pi q A_q^{\rm adj}}, \tag{73}$$

that for $q = 1$ yields

$$\gamma_{b,\text{v cone}} \simeq 121. \tag{74}$$

The buckling transition in the model of v-cones takes place at smaller FvK numbers, as compared to that in the standard model of circular cones with flat caps. The difference of (74) from the FvK buckling number (7) is physically due to different geometric structures accommodating the topological defects and used to ensure the balance of strain-bending energies upon buckling [209].

The resulting energy of the variable cones then simplifies to

$$\frac{G_{\text{shell,v cone}}}{\kappa} = \begin{cases} A_q^{\rm adj}\gamma + \frac{8\pi}{3}, & \gamma \leqslant \gamma_{b,\text{v cone}} \\ B_q^{\rm adj}\left(1-\sqrt{\frac{\gamma_{b,\text{v cone}}}{\gamma}}\right)^2 \log\left(\sqrt{\frac{\gamma}{\gamma_{b,\text{v cone}}}}+1\right) & \\ +\frac{72\bar{q}\beta_T^2}{\pi q}\left(\frac{3}{2}-\sqrt{\frac{\gamma_{b,\text{v cone}}}{\gamma}}\right)+\frac{8\pi}{3}, & \gamma > \gamma_{b,\text{v cone}}. \end{cases} \tag{75}$$

The comparison of Eq. (75), which is the main result of this section, with the computer-simulations data of Lidmar *et al.* [18] reveals a remarkable agreement in the regime of low-to-moderate FvK numbers, at $\gamma \lesssim 10^4$, as illustrated in Fig. 12, supporting our modified theoretical approach [210].

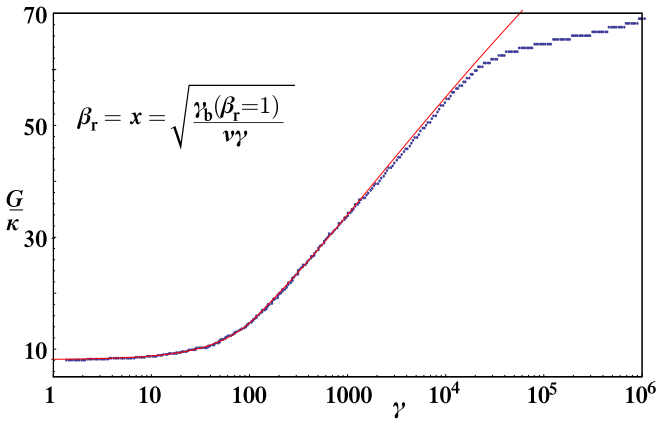

FIG. 12. Energy variation of the shell plotted using the simplified variable-cone analytical expression (75) (the thin solid red curve). The simulations data of Lidmar *et al.* [18] are the blue points.

III. TWO-COMPONENT SHELLS: RESULTS ON PROPAGATION AND STALLING OF THE SOFT MATERIAL

We describe below the two-component surfaces with different elastic moduli of their materials that require a more detailed understanding of the building up of strain and curvature. Following the physical concepts outlined in Sec. II C, here we develop a theoretical framework to calculate the energetics of realizable distributions of the soft-material component on the surface of a hard-material crystalline icosahedral shell. We consider a number of features of capsid "invasion" by the soft material leading to minimal-energy shapes with domes and cones partly filled by the soft phase. The soft phase is composed of a material with relatively small FvK numbers, much smaller those that for the hard material,

$$\gamma_s \ll \gamma_r, \tag{76}$$

i.e., with small ratios of the Young's to the bending modulus $K_s/\kappa_s \ll K_r/\kappa_r$.

A. Model, approximations, and geometry

We consider a hard-material shell with $12/q$ defects geometrically arranged into a polyhedron, with the shell containing a relatively small fraction f of the soft material. The quantities for the soft and rigid components are denoted by the subscripts "s" and "r," correspondingly. Note that at large-f values some stripelike and barrel-like structures can emerge as the energy-minimum conformations (see Refs. [178,180,182]). We suppose the shell surface is large enough, so that both rigid- and soft-material FvK numbers exceed the value for the respective buckling transition [211]), so that

$$\gamma_{(r,s)} > \gamma_b \approx 131. \tag{77}$$

We suppose that *no grain boundaries* [16,20,24] emerge along the interface of these two commensurate materials. The two phases can thus be connected together geometrically smoothly, but with a line-tension penalty along their contact boundary. The boundary features a line tension λ measured in units k_BT per length. For an area fraction f of the soft material in the shell, we investigate its distributions minimizing the total energy, depending on values of the elastic moduli and line tension λ.

The elastic moduli of the soft and rigid phases define the *dimensionless* radii of the respective buckling domes $\rho_{\text{dome}\,(r,s)}$

[using Eqs. (6) and (39)] and

$$x_{(r,s)} = \frac{\rho_{\mathrm{dome}\,(r,s)}}{R_{\mathrm{shell}}} = \sqrt{\frac{B_q^{\mathrm{adj}}\kappa_{(r,s)}}{2A_q^{\mathrm{adj}}K_{(r,s)}R_{\mathrm{shell}}^2}} = \sqrt{\frac{\gamma_b}{\gamma_{(r,s)}}}. \quad (78)$$

All lengths are scaled with the shell radius R_{shell}. For the soft material

$$x_s > x_r \quad (79)$$

and it is assumed to be spread over $n \leqslant 12/q$ domes.

The soft material first "invades" the rigid domes, the regions with the largest density of both the bending energy and strain. The "soft invasion" starts as a circular region around the center of a given defect: such circular domains minimize the line-tension penalty. Using Eq. (14) coupling r_{disk} and ρ_{dome} we define the generalized radius of the dome. For the soft material in the ith sector with the soft-phase fraction f_i this results in the scaled radius z_i defined via

$$(q\pi/3)(R_{\mathrm{shell}}z_i)^2 = f_i 4\pi R_{\mathrm{shell}}^2 \quad (80)$$

as

$$z_i = \sqrt{12 f_i/q}. \quad (81)$$

The icosahedral symmetry of the underlying surface is assumed in our model to be unaltered by the actual occupation of each defect-containing region by the soft material as well as by the overall distribution of the regions occupied by the soft phase. Each of the defects is thus fully independent with respect to its response to an increasing fraction of the soft material on the shell surface. The energetic balance of filling each defect-containing region by the soft phase is considered to be the same, with the total elastic energy required to be minimal. This approach allows for a tractable analytical solution for the sequence and extent of filling of domes and cones by the soft material in two-component shells.

From the biophysical perspective of viral-capsid formation, an increase of the soft-component fraction f on the shell can be mediated by several factors. The assembly process of two-component capsids is often an equilibrium process; some of its features can potentially be described in terms of a simple adsorption isotherm

$$\frac{\theta_{(r,s)}}{1-\theta_{(r,s)}} = \frac{c_{(r,s)}}{c_{\mathrm{water}}} \exp\left[-\frac{U_{(r,s)}^{\mathrm{bind}}}{k_BT}\right] \exp\left[-\frac{F_{\mathrm{ads}}}{k_BT}\right]. \quad (82)$$

Here, the molar concentrations of units of the soft and rigid components in the aqueous solution with $c_{\mathrm{water}} = 55$ M (acting as a reservoir of shell-building blocks) are, respectively, c_s and c_r. The coverage of all available "adsorption sites" (on the shell surface of a constant size) N_{ads} by N_s soft- and N_r rigid-component units are, respectively, $\theta_s = N_s/N_{\mathrm{ads}}$ and $\theta_r = N_r/N_{\mathrm{ads}}$. Here, $F_{\mathrm{ads}}(\theta_{(r,s)})$ is the general adsorption-free-energy term describing other possible and nonenergetic contributions to the adsorption process of subunits onto the shell. The increasing concentration of soft-component units in the solution (higher c_s values) as well as more profitable association energies of soft-component subunits on the shell (more negative U_s^{bind} values) will yield higher values of θ_s and, as a consequence, higher overall soft-component fractions f. In this picture, no interconversion of soft and rigid subunits is necessary on the shell surface, but rather the proper adsorption equilibrium is being established between the shell surface and bulk solution of subunits of both types.

From the mechanical perspective, as intuitively expected, smaller bending and stretching rigidities of the soft phase as well as smaller line-tension penalties to incorporate the soft phase into the shell surface will also give rise to larger fractions of the soft component f. Upon increase of f the shell surface itself is assumed not to change in the model and the soft component occupies the most "dense" shell regions from the viewpoint of elastic-energy density. We call this process "shell invasion" by the soft phase. The term invasion means a process of "replacement" of the rigid phase of the shell, which becomes progressively energetically unprofitable, by the soft phase in the course of, e.g., a process of equilibrium shell self-assembly from elementary units in the solution [see, e.g., Eq. (82)].

B. Stages of invasion and energy calculations

We distinguish *three stages* of sector invasion by the soft material, taking place for an increasing soft-phase surface occupancy f. Stage I: The soft material invades and replaces the rigid-material region in the dome, starting from the defect. Stage II: The dome consisting of only soft material grows in size until z_i reaches x_s, thereby replacing the rigid material from the cone surface. Stage III: The soft material invades the remaining cone until its maximal size (defined by the overall shell size) is achieved. The resulting line-tension energetic penalty depends only on z_i, but not on the stage of invasion, namely,

$$S_{\mathrm{line}}(z_i) = \lambda(\pi/3)\sqrt{2q\bar{q}}R_{\mathrm{shell}}z_i. \quad (83)$$

Subtracting the basal energy of a purely rigid sector, we evaluate the change in the elastic energy, for each stage of invasion. The results are summarized in Table III.

To simplify the analysis, we scale the total energy in the units of $qB_q^{\mathrm{adj}}\kappa_r/24$ [chosen to simplify the general results for $\mathcal{E}(\nu)$ below] and change from the soft-fraction parameter z_i in Eq. (81) to the respective level of invasion of the ith sector, denoted by

$$\nu(f_i) = (z_i(f_i)/x_r)^2. \quad (84)$$

The resulting *dimensionless* energy is defined as

$$\mathcal{E}(f) = 24G(f)/\left(qB_q^{\mathrm{adj}}\kappa_r\right), \quad (85)$$

where $G(f)$ is the total energy of the shell with the soft-phase fraction f (see the results in Table III). For these soft-material fillings, we compute the energy difference relative to the energy of the rigid shell at $f = 0$ for the three different regions of soft-material occupancy ν as follows

$$\mathcal{E}(\nu) = n\left[(\Gamma\Delta - 1)\nu + \Lambda\sqrt{\nu} + 16\pi(\Delta - 1)\nu/B_q^{\mathrm{adj}}\right], \ \nu \leqslant 1, \quad (86)$$

$$\mathcal{E}(\nu) = n\left[(\Gamma\Delta\nu - 1) + \Lambda\sqrt{\nu} - \log\nu + 16\pi(\Delta - 1)/B_q^{\mathrm{adj}}\right], \quad 1 \leqslant \nu \leqslant 1/\Gamma, \quad (87)$$

TABLE III. Changes of the elastic energy upon addition of the soft material to the rigid-material shell, per each sector containing one defect. The results were obtained using Eqs. (25), (31), and (36) for the energy contributions of the rigid (subscript "r") and soft ("s") components, with z_i defined in Eq. (81). The energy change depends on the stage of invasion by the soft phase (see text for details).

Stage of invasion	Strain energy, dome	Bending energy, dome	Bending energy, cone
I	$\frac{qA_q^{\rm adj}}{12}[\gamma_s\kappa_s-\gamma_r\kappa_r]z_i^2$	$(\kappa_s-\kappa_r)\frac{2q\pi}{3}\frac{z_i^2}{x_r^2}$	0
II	$\frac{qA_q^{\rm adj}}{12}[\gamma_s\kappa_s z_i^2-\gamma_b\kappa_r]$	$(\kappa_s-\kappa_r)\frac{2q\pi}{3}$	$\frac{q}{12}B_q^{\rm adj}\kappa_r\log\left[\frac{x_{\rm dome}}{z_i}\right]$
III	$\frac{qA_q^{\rm adj}}{12}\gamma_b[\kappa_s-\kappa_r]$	$(\kappa_s-\kappa_r)\frac{2q\pi}{3}$	$\frac{qB_q^{\rm adj}}{12}\left(\kappa_s\log\left[\frac{z_L}{x_s}\right]-\kappa_r\log\left[\frac{z_L}{x_r}\right]\right)$

and

$$\mathcal{E}(\nu)=n\big[(\Delta-1)+\Lambda\sqrt{\nu}+\Delta\log\Gamma +(\Delta-1)\log\nu+16\pi(\Delta-1)/B_q^{\rm adj}\big],\quad \nu\geqslant 1/\Gamma. \tag{88}$$

The three dimensionless model and material parameters used in these expressions are as follows: the ratio of the FvK numbers of both materials

$$\Gamma=\gamma_s/\gamma_r, \tag{89}$$

the ratio of their bending moduli [84]

$$\Delta=\kappa_s/\kappa_r, \tag{90}$$

and the renormalized line-tension parameter between the two phases

$$\Lambda=\frac{8\pi}{B_q^{\rm adj}}\sqrt{\frac{2\gamma_b\bar{q}}{qK_r\kappa_r}}\lambda. \tag{91}$$

Note that all these *dimensionless* parameters have no explicit dependence on the shell size $R_{\rm shell}$ [the shell is large enough for both materials to be in their buckling range, see Eq. (77)]. The energy relations (86)–(88) are the main results of this section: they govern the energetics of invasion of the rigid-crystalline icosahedral shell by the soft material.

Let us turn to the detailed analysis of invasion, with some relevant and auxiliary results collected in Table IV. As we are interested for the system's configurations with the lowest total energy, only such values of ν are allowed that yield negative values of $\mathcal{E}$. We find, in particular, that the line-tension energy accompanying the inclusion of each soft-material domain into the shell prevents the invasion in stage I at small fractions f, as physically expected. The minimal f needed before the invasion of the first sector starts is $\nu_{\rm start}(1)$ (see Table IV). As we have $\nu\leqslant 1$ in stage I, the line tension has an upper limit Λs_{12} above which a partial invasion of the rigid dome is not possible and the invasion starts in stage II. The energy curve has then only one minimum at $\nu_{\rm min}$ in either stage II or III, depending on whether Λ is correspondingly larger (the minimum is in stage II) or smaller (the minimum is in stage III) than Λm_{23} (see Figs. 13 and 14). The invasion of the soft material can never go beyond this minimum. The boundaries for Λ are partly overlapping being useful in certain combinations: for example, to have an accessible minimum in stage II the line-tension parameter Λ should be limited by

$$\Lambda m_{12}<\Lambda\leqslant\Lambda m_{23} \tag{92}$$

and $\Lambda<\Lambda_2$. At the onset of stalling, the gain from expanding a soft dome at the expense of the added soft material is smaller than the energy losses due to a higher line-tension contribution. This explains the existence of certain energetic barriers in Fig. 13(c) in the blue shaded regions.

C. Sector-by-sector invasion and stalling

One can show that the energy curve in stage I is concave, while in stages II and III up to the point $\nu=\nu_{\rm min}$ it is

TABLE IV. Physical meaning of some of the variables determining the soft-material invasion of the rigid shell.

Symbol	Value/expression	Physical meaning
Λm_{23}	$2\sqrt{\Gamma}(1-\Delta)$	Boundary for Λ of $\nu_{\rm min}$ in stage II or III
Λm_{12}	$2(1-\Gamma\Delta)$	Boundary for Λ of $\nu_{\rm start}$ in stage I or II
Λ_1	$1-\Delta\Gamma+(1-\Delta)\frac{16\pi}{B_q^{\rm adj}}$	Upper bound for $\nu=1$ to have $\mathcal{E}<0$
Λ_2	$2\sqrt{\Gamma\Delta}\left(\frac{1}{\sqrt{{\rm W_p}(a)}}-\sqrt{{\rm W_p}(a)}\right)$,	Upper bound for $\mathcal{E}[\nu_{\rm min}(2)]<0$
	where $a=\Gamma\Delta\exp\left[1-\frac{16\pi}{B_q^{\rm adj}}(1-\Delta)\right]$	and ${\rm W_p}(...)$ is the Lambert W function
Λ_3	$2(1-\Delta)\Gamma^{-\frac{\Delta}{2(1-\Delta)}}\exp\left[\frac{8\pi}{B_q^{\rm adj}}-\frac{1}{2}\right]$	Upper bound for $\mathcal{E}[\nu_{\rm min}(3)]<0$
$\nu_{\rm start}(1)$	$\frac{16\pi}{B_q^{\rm adj}}(1-\Delta)+1-\Gamma\Delta$	Starting level of invasion for stage I
$\nu_{\rm max}$	$\left(\frac{\Lambda B_q^{\rm adj}}{32\pi(1-\Delta)+2B_q^{\rm adj}(1-\Gamma\Delta)}\right)^2$	Maximum level of invasion in stage I
$\nu_{\rm min}(2)$	$\left(\frac{\sqrt{\Lambda^2+16\Gamma\Delta}-\Lambda}{4\Gamma\Delta}\right)^2$	$\nu_{\rm min}$ for invasion in stage II
$\nu_{\rm min}(3)$	$\left(\frac{2(1-\Delta)}{\Lambda}\right)^2$	$\nu_{\rm min}$ for invasion in stage III

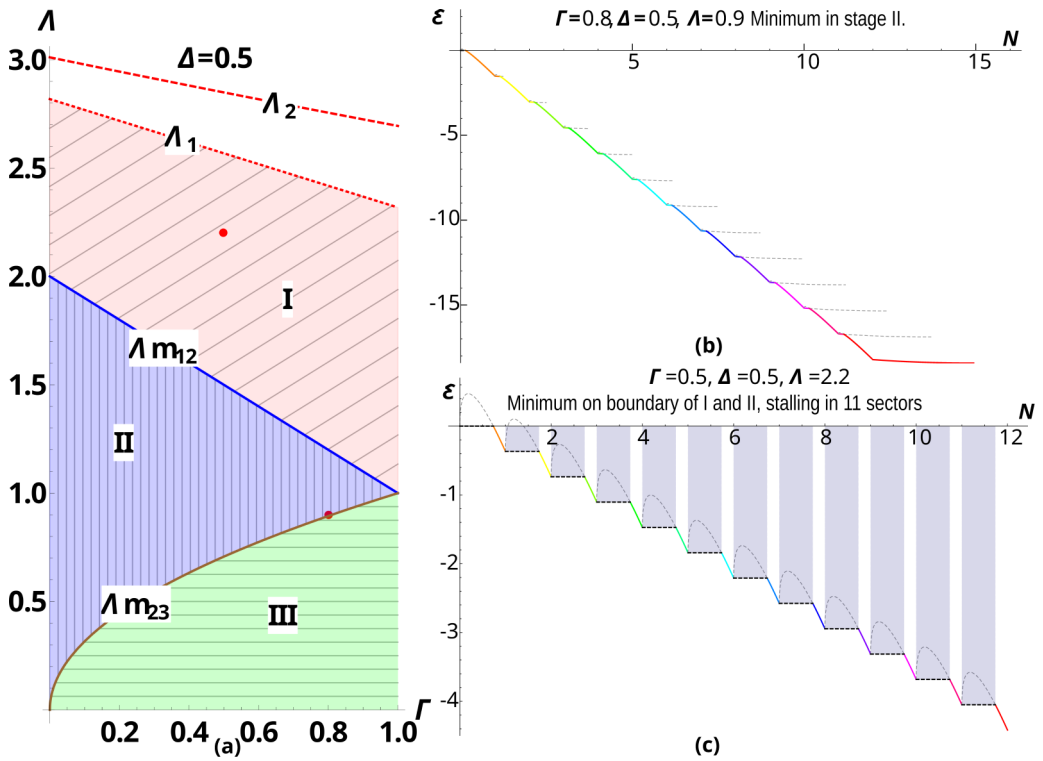

FIG. 13. (a) Filling configurations by the soft material in the $\{\Gamma - \Lambda\}$ plane, with the different colors filling the regions of occupation in stages I, II, and III, as denoted in the plot (see also Table IV for details). The two red dots in (a) designate the values of parameters used to compute the results presented in (b) and (c), as indicated in the legend. The boundary curves $\Lambda(\Gamma)$ between the stages I, II, and III of invasion illustrated in (a) are explained in Table IV. (b), (c) The minimal energy curves $\mathcal{E}(n)$ as given by Eqs. (86)–(88) plotted versus the number $n = 1, 2, \ldots, 12$ of defect-centered segments filled by the soft material, plotted for the model parameters Γ in Eq. (89), Δ in Eq. (90), and Λ in Eq. (91) as indicated in the legend. The fraction f in (b) and (c) increases as the soft material continuously fills the shell. In (c) this filling happens in a cone up to a point when the filling stalls, while f increases up to a level when the next cone starts filling in the energy-minimum state, etc. Different colors of the curves in (b) and (c) denote additional different sectors being invaded or filled by the soft material, while the dotted lines in (c) denote the energy *increase* (not realizable in the ground state of the system). The dashed black horizontal lines in (c) extending into the vertical gray-bluish strips are the stalling intervals of invasion.

convex. As an important consequence, in the ground state there exists either one partially invaded stage-I sector and all other invaded sectors are at the level of filling $\nu = 1$, or the invaded sectors are all at the same level of filling by the soft material $1 < \nu \leqslant \nu_{\min}$. Since the elastic-energy density is the highest in the domes, these are the only energetic configurations we need to consider. Suppose that n sectors of the shell are invaded by the soft material up to a level $\nu \geqslant 1$. A new sector gets invaded when n sectors are filled so far that the increase in energy is compensated by the decrease in energy from the material invading a new sector.

1. Energetics of soft-material invasion

The jump levels at which the invasion of a new sector takes place, denoted below as $\nu_{\text{jump}}(n)$, are defined via the energy relations

$$n\mathcal{E}(\nu_{\text{jump}}(n)) = (n+1)\mathcal{E}(\nu_{\text{start}}(n+1)) \tag{93}$$

with $\mathcal{E}(\nu_{\text{start}}(n+1)) = \mathcal{E}(\frac{n}{n+1}\nu_{\text{jump}}(n))$ if $n\nu_{\text{jump}}(n) \geqslant n+1$ and

$$n\mathcal{E}(\nu_{\text{jump}}(n)) = \mathcal{E}(\nu_{\text{start}}(n+1)) + n\mathcal{E}(1) \tag{94}$$

with $\mathcal{E}(\nu_{\text{start}}(n+1)) = \mathcal{E}(n\nu_{\text{jump}}(n) - n)$ if $n\nu_{\text{jump}}(n) < n+1$. Again, there is a line-tension barrier to overcome, but since the soft material for invading a new sector is taken from the other already invaded sectors, the starting value is

$$\nu_s(n+1) \geqslant \nu_s(n). \tag{95}$$

In fact, we can show that

$$\nu_{\text{jump}}(n+1) \leqslant \nu_{\text{jump}}(n) \tag{96}$$

and

$$\nu_{\text{start}}(n+1) \geqslant \nu_{\text{start}}(n). \tag{97}$$

The equality sign for these two relations is only realized when the minimum is at

$$\nu_{\min} = 1 \tag{98}$$

and the starting value is at $\nu_{\text{start}}(n) = \nu_{\text{start}}(1)$ for all values of n.

This situation is illustrated Figs. 13(b) and 13(c). The length of the energy plateau in Fig. 13(c), the so-called stalling length, remains constant for each new sector of the soft material being added to the shell. In the extreme form of stalling, when the invasion stalls before the beginning a new sector until there is enough soft material to invade the new sector

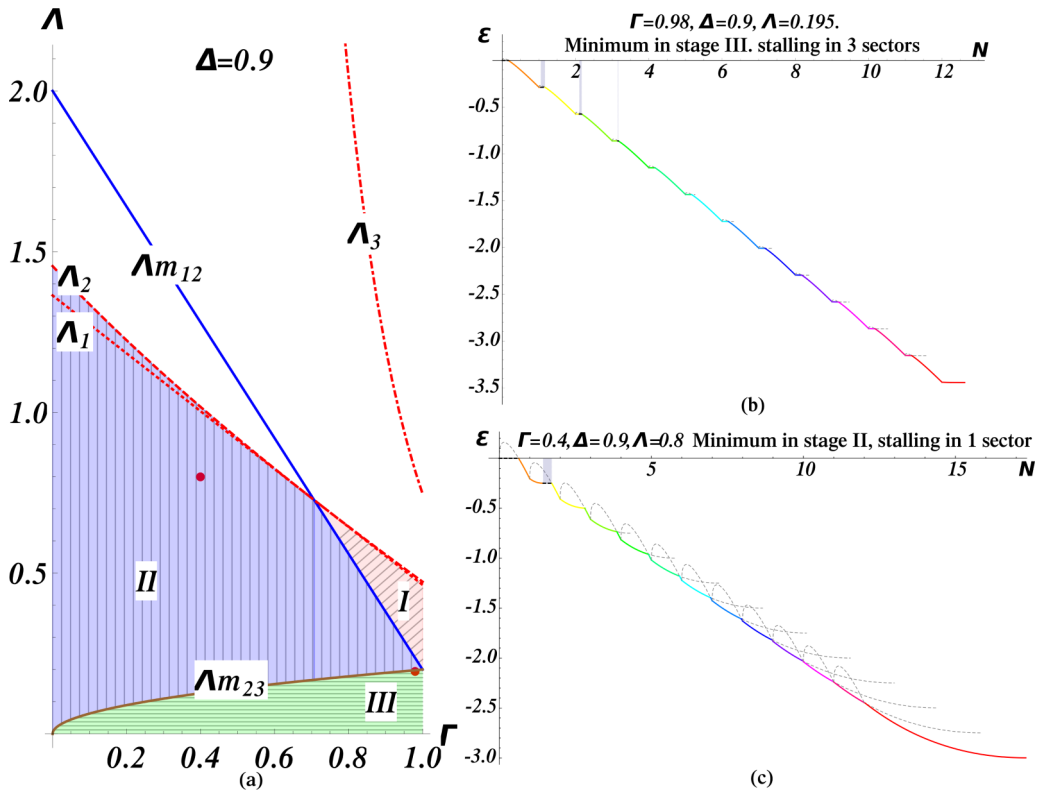

FIG. 14. The same quantities as in Fig. 13, with the same notations for the curves in the respective panels, but for the case when the bending moduli of the two phases are close, at $\Delta = 0.9$. Here, both energy plots in (b) and (c) stall for only very small sectors (see the thin shaded regions): one of them is in stage II and the other one is in stage III. Note that when $\Lambda < \Lambda m_{23}$ the minimum is in stage III and the energy is always negative.

up to the starting level $\nu_{\rm start}(1)$. When the minimum is not at the level (98), the stalling decreases since the level $\nu_{\rm start}(n)$ increases with n. Depending on the model parameters, the stalling might disappear before all the sectors are invaded by the soft material and the values $\nu_{\rm start}(n+1)$ and $\nu_{\rm jump}(n)$ approach each other.

For any finite line tension λ there exists a minimal fraction of the soft material before the invasion of the first sector starts. The energy profile is found to have one minimum that can be situated in stages II or III (see Fig. 13). Further invasion by the soft material will cost more energy as compared to the case of no new material being added the rigid shell at all. When the invasion of sectors reaches this minimum, the only energetically viable option for the soft material is to start invading a second sector (that is not always possible because of a finite initial line-tension penalty). This stalling of invasion decreases usually with the number of sectors already invaded. If the line tension is low enough, that invasion of the nth sector is in stage I, then this invasion happens with all $(n-1)$ already invaded sectors at the boundary of stages I and II. Otherwise, all n sectors are at the the same level in stage II or III.

The energy minimum in stage III is, naturally, only possible when

$$\kappa_s < \kappa_r, \tag{99}$$

but the line tension needs to be low enough for this to happen [compare the invasion diagrams in panel (a) and the energy curves in panels (b) and (c) of Figs. 13 and 14]. These two figures illustrate the model predictions for two different values of the ratio of the bending moduli Δ, namely, for $\Delta = 0.5$ in Fig. 13 and for $\Delta = 0.9$ in Fig. 14. We observe that when the invasion of the first sector reaches the energy minimum, the only remaining option upon increase of fraction f is to start the invasion of one more sector of the rigid shell. The start of this process is, however, penalized by a finite line-tension energy. The process of "stalling invasion" corresponding to the increase of the total energy [see the gray shaded regions in Fig. 13(c)] gets reduced with the number of sectors already occupied by the soft phase. Note that at $\Delta = 1$ the bending moduli of the soft and rigid materials are the same and, thus, no invasion of the cones is possible in the energy-minimum state. This is because no gain in the bending energy would come from replacing the rigid material by the soft phase in the cones, while certain losses in the growing line-tension energy are inevitable. Therefore, the cones stay rigid in stage III of the invasion under the condition $\kappa_r = \kappa_s$.

Although the total energy of the system in the lowest-energy state is a multivalued function revealing discontinuous jumps as a function of the number of soft-phase-occupied defect-containing regions n, we expect this system to reveal no hysteretic behavior. Upon decrease of f the system will follow the same "energetic" ground-state path, so that no hysteresis occurs. However, if one could gradually change the fraction ν in Eq. (84) while dynamically "updating" the optimal shell structures, the question of possible hysteresis could become

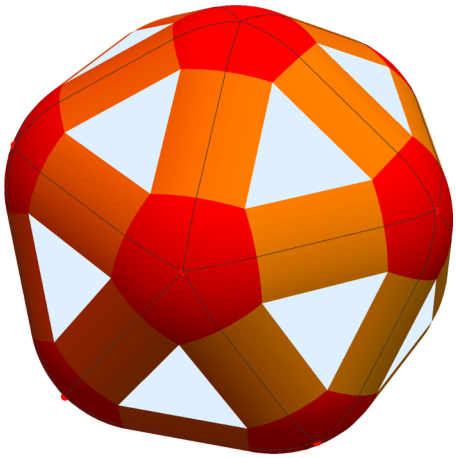

FIG. 15. Buckling of a spherical shell into the domes connected by the cylindrical segments and flat triangular faces. This dome-face-ridge simplified model for FvK numbers above buckling is a "predecessor" of the variable-cone model (see Sec. III C 1 for details).

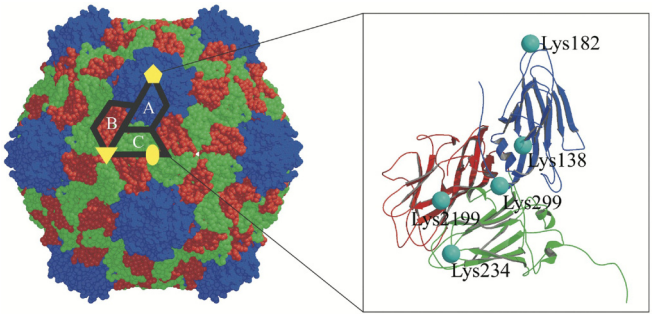

FIG. 16. Viral capsid and asymmetric unit of Cowpea Mosaic Virus (CPMV), as reproduced from Ref. [32] (where the detailed explanation of the components is given). We acknowledge the permission from Elsevier to reuse this figure without charges.

relevant. Here, we have a fixed ν in the solution and check the ground-state structures. The appearance of each additional domain invaded by the soft material is penalized by a certain line-tension energy creating the discontinuous jumps in the dependence of the total energy versus the number of invaded domains. Thus, the system will likely follow the same path as the number of domains n is being reduced when the fraction f drops and as n increases when f grows.

2. *Edge invasion*

The process of edge invasion is based on the model of variable cones. We assume that the dome size and the radius of the related cylindrical segment are set by the material occupying the dome according to

$$\rho_{\text{dome}} = \sqrt{\gamma_{b,\text{v cone}}/\gamma} \times R_{\text{shell}}. \tag{100}$$

We allow the cylindrical segment angle β_{rel} to only have a lower bound of $\rho_{\text{dome}}/R_{\text{shell}}$. The idea is that the invading material has a lower bending modulus, not necessarily a lower FvK number, driving a transfer of bending from the cones to the edges (see an exemplary configuration in Fig. 15). This gives us a qualitative picture of edge invasion.

IV. DISCUSSION AND CONCLUSIONS

A. Summary of the main results for single- and two-component shells

The incompatibility of planar hexagonal packing with the wrapping of a crystalline sheet of material into a closed surface inevitably implies the formation of at least 12 topological defects to optimize the bending-versus-stretching energy contributions of the shell. In this study, we presented a number of analytical results regarding the buckling transition in the spherical geometry, with applications to shape deformations and energetics of rigid liquid-crystalline icosahedral shells.

First, we improved the well-recognized analytical description of the energetics of buckling for rigid icosahedra [14,16–19]. Our cone-and-dome-based modifications provided a good agreement for the shell energetics with the data obtained from computer simulations [18]. A faceting transition along flat faces of variable cones connected by cylindrical segments was also described.

Next, we examined the energetics of two-component shells and quantified how the elastic energy of the topological defects on an icosahedron gets reduced via introducing a soft elastic component on the shell. We rationalized how the soft material invades the regions with the highest elastic-energy density, occupying the defects of icosahedra first. We quantified how the radius of these spherical caps grows with the amount of added soft material and how the elastic energy of the entire shell decreases with the number of defects occupied by the soft component. We examined the effects of varying line tensions between the soft and rigid phases, shell dimensions, and Young's moduli of the two materials onto the shell energetics.

We also computed the phase diagram of the system and rationalized how the consecutive filling of domes on the buckled icosahedral structure takes place, for the situations with and without a stalling of soft invasion. Physically, the above mentioned stalling process means that for some region of the system parameters, the total elastic energy of the shell stops decreasing upon addition of the soft component to its surface, staying rather constant before the next defect gets invaded by the soft component at an increasing soft-phase occupancy f. During stalling, it becomes energetically favorable not to include more soft material, although its concentration in the solution increases, with f being naturally connected to it via an adsorption isotherm.

We explored the energetics of the buckling transition of a cone via introducing the picture of the cylindrical segments connecting the domes on the surface of an icosahedron. This *variable-cone* modification of the circular-cone picture of the established shell-buckling models [17,18] enabled us to achieve a better agreement with the results of computer simulations for the elastic energy of icosahedral shells versus the FvK number, both prior to and after the buckling transition.

For a single-component shell, the geometric shape of variable cones provides a self-consistent description of buckling.

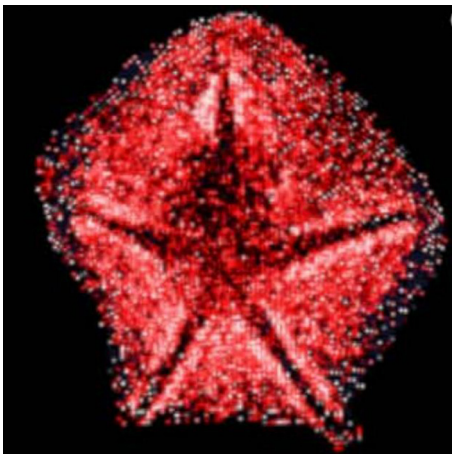

FIG. 17. Pentagonal "stargate" on one vertex of the mimivirus. The image is reproduced from Ref. [40].

For a two-component capsid, the previously unexplored buckling mechanism and its boundaries (stages of invasion) are rationalized analytically. The respective phase diagrams in terms of relative values of the bending stiffness and Young's modulus of the rigid and soft phases are computed. In the future, we plan to use this variable-cone model to examine the energetics of *ridge filling* on the capsids by the soft phase, to improve the current two-component shell results of Sec. III A where filling was limited to domes and growing cones.

Methodologically, the current investigation is reminiscent of the numerical energy minimization of Refs. [83–85], where two-component irregular polyhedral shells were studied. With the first component (the rigid phase) favoring the icosahedral geometry and the soft component preferring the sphere as the ground state, a large variety of possible energy-minimal (often irregular) phase distributions were computed [83–85]. The preference for each of these structures changes with varying fraction of occupancy of the shell by the soft component and different bending and stretching moduli of both components. The general trend is that the hardly bendable phase naturally prefers to occupy the most flat facets of these irregular polyhedral shells, while a hardly stretchable but easily bendable phase fills the ridges. Segregation of each component into their bending-plus-stretching energy preferable domains is penalized by possible line-tension energies that disfavor small domains (setting a minimal domain size) and, thus, yield a smaller number of domains [83–85].

B. Biological and biomedical relevance

From the biological perspective, the understanding of the buckling transitions taking place in various viral capsid shells (see Fig. 16) [9,18] is of great importance, e.g., for possible engineering of nanocontainers for material science, with a number of biomedical and biotechnological applications. Viral capsids are, for instance, the main players in transporting the genetic material and other cargos into host cells for viral-based gene-therapy applications [212–214]. Viral vectors derived from certain modified retroviruses, adenoassociated virus, herpes virus, and pox virus are the main virus families employed in the clinical gene therapy of cancer [215,216]. The release of encapsulated genetic material from a rather stable capsid, often a problem for achieving high transfection efficiencies of gene transfer, might be facilitated via introducing a soft and less stable component onto the shell surface, as we examined above.

Also note that the filling of domes and ridges by the soft component for larger shells might provide a tempting explanation of a fivefold stargate formation near the vertex of the mimivirus [40,170,171] (see Fig. 17) [217]. The stargate structure is the most unstable region of the shell: the virus consistently undergoes rupture upon heating only in this region [40,218]. Following the stargate rupture and fusion of the internal membrane with the phagosome membrane, one plausible mechanism of DNA release is that the internal protein core enclosing the viral DNA is released from the capsid into the host cytoplasm along this membranous "infection channel" [218]. In the process of DNA ejection, five pentagonal faces of the mimivirus belonging to the unique, single vertex (see Fig. 17), open up and release the DNA into the amoebae cytoplasm via the stargate portal [40,171]. The edges of the stargate contain a ridge different from other edges of the capsid: the mimivirus capsid seems to be designed to be breakable and openable along these structural elements. The ease of opening of mimivirus capsids along the stargate edges (see Fig. 17) can be physically interpreted as a more

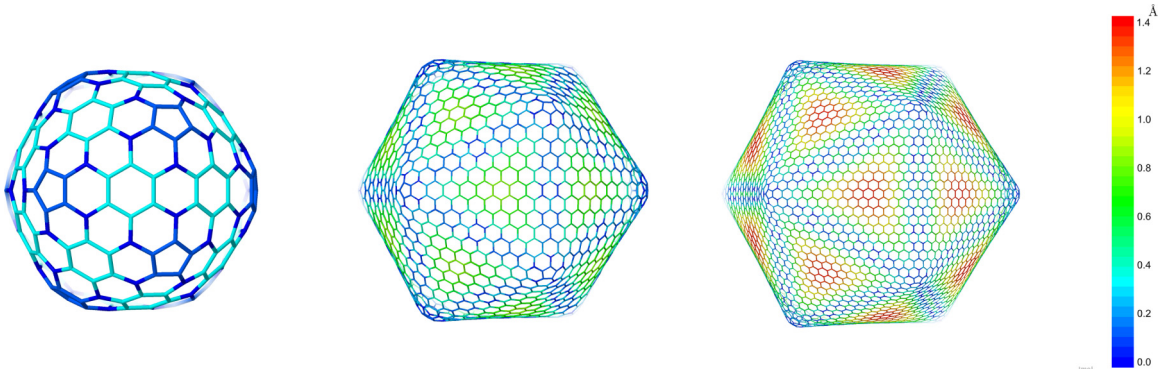

FIG. 18. Fullerenes of increasing generation-number demonstrate the polyhedral faceting transition, with $n_{\text{full}} = 2$, 6, and 10 structures shown in the plot (from left to right). The color scheme quantifies the displacements in atomic positions with respect to an ideally flat graphene triangle (see Ref. [7] for more details). The image is reproduced from Ref. [7], with permission from the PCCP Owner Societies.

elastically stretchable and breakable material occupying these edges. This supports the biophysical and biological relevance of our model of two-component shells, with the soft component invading the edges (see Fig. 15).

Note that the stable assembly of icosahedral viral capsids of different sizes (or, of different triangulation numbers $\mathcal{T}$ [3,9,35,105]) from the same protein subunits may not always be possible [219]. The concept of triangulation also limits the geometrically allowed number of protein subunits on a capsid to a discrete set of numbers

$$n_{\text{subunit}} = 60\mathcal{T} \tag{101}$$

(with some exceptions, see Ref. [9]), with the triangulation numbers $\mathcal{T} = 1, 3, 4, 7, 9, \ldots$ [220]. After an infection event *in vivo* and upon self-assembly *in vitro*, for a majority of spherical viruses the capsids are spontaneously formed into infectious virions monodisperse in size [69]. Some exceptions of *polymorphic* capsid-size assembly are however realizable, as discussed in Refs. [80,93,100,101,108,109,113,214,221]. Moreover, in trying to build shells of larger dimensions (or triangulation numbers $\mathcal{T}$ [9,35,100]) from the same elements, the interaction energies of subunits in progressively sharpening edges of the shell might acquire dihedral/hinge angles not commensurate with the (optimal) adhesiveness of their contacts (see the discussion in Refs. [29,30,69,80,81,100,101,105]). This fact renders the resulting structure less stable (or turns them unstable). We also emphasize that, as shown in Fig. 16, the elementary subunits of many viral-capsid proteins can be asymmetric in form, heterogeneous in protein composition, and nontrivial in their mutual interactions [3,9,28,29,31,97]. These features *per se* may severely impact the icosahedral appearance of some capsids (with planar tilings [222,223], e.g., being impossible to construct from these asymmetric structural elements).

C. Polyhedral faceting of giant fullerenes

Reiterating on fullerenes mentioned in the Introduction and depicted in Fig. 18, the required mechanical properties of extremely limited in-plane stretchability and comparatively easy bending are well satisfied for graphene monolayers [224]. The graphene sheets, single-walled carbon nanotubes, and spherical fullerenes are among the stiffest materials known, with the Young's moduli of 0.5…1 TPa [11,225,226]. With the in-plane-inextensibility constraint applied to fullerenes, the elastic energy of 12 conelike pentagonal disclinations constructing the entire fullerene shell was shown to have a logarithmic dependence on the shell size [7,227,228]. The excess energy, per C atom,

$$\Delta E_{\text{C}}(n_{\text{C}}) \sim \kappa_{\text{C}} \frac{11\pi}{5} \frac{\log\left[n_{\text{C}}/60\right]}{n_{\text{C}}}, \tag{102}$$

was shown to be in good agreement with the results of *ab initio* calculations [7]. The polyhedral faceting predicted for large and giant fullerenes [7,227,229–232] is thus similar to the faceting transition known for icosahedral viral capsids [9].

The energetics of icosahedrally shaped fullerenes with up to $n_{\text{C}} = 6000$ atoms was investigated via *ab initio* quantum-mechanical simulations [7]. The perfectly spherical appearance of the smallest C_{60} fullerene changes dramatically for larger fullerenes, which reveal a sharp-edge, gradually aspherical polyhedralike shapes (see Fig. 5 in Ref. [7] and Fig. 18). Moreover, the edges of the optimal-energy giant fullerene icosahedra feature a slight longitudinal *inward curvature* increasing with

$$n_{\text{C}} = 60 n_{\text{full}}, \tag{103}$$

while the faces are almost flat, with a slight *outward curvature* [7]. Here, n_{full} is the generation of fullerenes. Simultaneously, the excess energy per atom in polyhedral fullerenes (as compared that in a flat graphene sheet) decreases with the number n_{C} of carbon atoms according to Eq. (102) [7].

This is consistent, both qualitatively and quantitatively [7], with the predictions of the continuum elasticity theory of disclinations [17,18]. As a possible reason for a measurable discrepancy of the best-fit results for graphene's bending and flexural elasticity κ_{C}, the authors of Ref. [7] proposed a *neglected fivefold symmetry* around each disclination. This is exactly the topic of our current study, with the concept of variable cones introduced and developed to improve the geometrical representation and accuracy of the classical energy calculations [17] based on cones with circular cross sections.

ACKNOWLEDGMENTS

The authors thank M. De La Pierre for providing the high-quality version of Fig. 18, originally created by Y. Noel for Ref. [7]. A.G.C. thanks A. Minsky, R. Sknepnek, and G. Vernizzi for stimulating correspondence. We acknowledge funding from the Deutsche Forschungsgemeinschaft (DFG Grants No. CH 707/2-2 and No. CH 707/5-1 to A.G.C. and DFG Grant No. ME 1535/7-1 to R.M.). R.M. also acknowledges the Foundation for Polish Science (Fundacja na rzecz Nauki Polskiej, FNP) for support within an Alexander von Humboldt Honorary Polish Research Scholarship.

[1] Plato, "The Timaeus", 53c (ca. 360 B.C.).

[2] R. W. Marks, *The Dymaxion World of Buckminster Fuller* (Reinhold, NY, 1960).

[3] A. Siber, Icosadeltahedral geometry of geodesic domes, fullerenes and viruses: A tutorial on the T-number, Symmetry **12**, 556 (2020).

[4] H. W. Kroto, J. R. Heath, S. C. O'Brien, R. F. Curl, and R. E. Smalley, C_{60}: Buckminsterfullerene, Nature (London) **318**, 162 (1985).

[5] H. Kroto, Symmetry, space, stars and C_{60}, Rev. Mod. Phys. **69**, 703 (1997).

[6] B. Kostant, Structure of the truncated icosahedron (such as fullerene or viral coatings) and a 60-element conjugacy class in $PSl(2, 11)$, Proc. Natl. Acad. Sci. USA **91**, 11714 (1994).

[7] Y. Noel, M. De La Pierre, C. M. Zicovich-Wilson, R. Orlando, and R. Doves, Structural, electronic and energetic properties of giant icosahedral fullerenes up to C6000: insights from an

ab initio hybrid DFT study, Phys. Chem. Chem. Phys. **16**, 13390 (2014).

[8] P. Schwerdtfeger, L. N. Wirz, and J. Avery, The topology of fullerenes, WIREs Comput. Mol. Sci. **5**, 96 (2015).

[9] T. S. Baker, N. H. Olson, and S. D. Fuller, Adding the third dimension to virus life cycles: Three-dimensional reconstruction of icosahedral viruses from cryo-electron micrographs, Microbiol. Molec. Biol. Rev. **63**, 862 (1999).

[10] M. D. Spivak, *A Comprehensive Introduction to Differential Geometry* (Publish or Perish Press, Houston, 1979).

[11] M. J. Bowick and L. Giomi, Two-dimensional matter: order, curvature and defects, Adv. Phys. **58**, 449 (2009).

[12] M. J. Bowick and R. Sknepnek, Pathways to faceting of vesicles, Soft Matter **9**, 8088 (2013).

[13] J. M. Kosterlitz and D. J. Thouless, Ordering, metastability and phase transitions in two-dimensional systems, J. Phys. C: Solid State Phys. **6**, 1181 (1973).

[14] M. J. Bowick, D. R. Nelson, and A. Travesset, Interacting topological defects on frozen topographies, Phys. Rev. B **62**, 8738 (2000).

[15] G. Vernizzi and M. O. de la Cruz, Faceting ionic shells into icosahedra via electrostatics, Proc. Natl. Acad. Sci. USA **104**, 18382 (2007).

[16] M. J. Bowick and A. Travesset, The statistical mechanics of membranes, Phys. Rep. **344**, 255 (2001).

[17] H. S. Seung and D. R. Nelson, Defects in flexible membranes with crystalline order, Phys. Rev. A **38**, 1005 (1988).

[18] J. Lidmar, L. Mirny, and D. R. Nelson, Virus shapes and buckling transitions in spherical shells, Phys. Rev. E **68**, 051910 (2003).

[19] T. A. Witten, Stress focusing in elastic sheets, Rev. Mod. Phys. **79**, 643 (2007), and references cited therein.

[20] S. Guttman, B. M. Ocko, M. Deutsch, and E. Sloutskin, From faceted vesicles to liquid icoshedra: Where topology and crystallography meet, Curr. Opin. Colloid Interface Sci. **22**, 35 (2016).

[21] E. L. Altschuler, T. J. Williams, E. R. Ratner, F. Dowla, and F. Wooten, Method of Constrained Global Optimization, Phys. Rev. Lett. **72**, 2671 (1994).

[22] E. L. Altschuler, T. J. Williams, E. R. Ratner, R. Tipton, R. Stong, F. Dowla, and F. Wooten, Possible Global Minimum Lattice Configurations for Thomson's Problem of Charges on a Sphere, Phys. Rev. Lett. **78**, 2681 (1997).

[23] M. J. Bowick, A. Cacciuto, D. R. Nelson, and A. Travesset, Crystalline Order on a Sphere and the Generalized Thomson Problem, Phys. Rev. Lett. **89**, 185502 (2002).

[24] A. R. Bausch, M. J. Bowick, A. Cacciuto, A. D. Dinsmore, M. F. Hsu, D. R. Nelson, M. G. Nikolaides, A. Travesset, and D. A. Weitz, Grain boundary scars and spherical crystallography, Science **299**, 1716 (2003).

[25] W. H. Roos, R. Bruinsma, and G. J. L. Wuite, Physical virology, Nat. Phys. **6**, 733 (2010).

[26] A. Siber, A. L. Bozic, and R. Podgornik, Energies and pressures in viruses: contribution of nonspecific electrostatic interactions, Phys. Chem. Chem. Phys. **14**, 3746 (2012).

[27] Z. Chen *et al.*, Protein-RNA interactions in an icosahedral virus at 3.0 Å resolution, Science **345**, 154 (1989).

[28] M. G. Rossmann and J. E. Johnson, Icosahedral RNA virus structure, Annu. Rev. Biochem. **58**, 533 (1989).

[29] V. S. Reddy, H. A. Giesing, R. T. Morton, A. Kumar, C. B. Post, C. L. Brooks III, and J. E. Johnson, Energetics of quasiequivalence: computational analysis of protein-protein interactions in icosahedral viruses, Biophys. J. **74**, 546 (1998).

[30] V. S. Reddy *et al.*, Virus particle explorer (VIPER), a website for virus capsid structures and their computational analyses, J. Virology **75**, 11943 (2001).

[31] L. Tang, K. N. Johnson, L. A. Ball, T. Lin, M. Yeager, and J. E. Johnson, The structure of Pariacoto virus reveals a dodecahedral cage of duplex RNA, Nat. Struct. Biol. **8**, 77 (2001).

[32] A. Chatterji, W. F. Ochoa, M. Paine, B. R. Ratna, J. E. Johnson, and T. Lin, New addresses on an addressable virus nanoblock: Uniquely reactive Lys residues on Cowpea Mosaic Virus, Chem. Biol. **11**, 855 (2004).

[33] A. G. Cherstvy, Electrostatic interactions in biological DNA-related systems, Phys. Chem. Chem. Phys. **13**, 9942 (2011).

[34] F. H. C. Crick and J. D. Watson, Structure of small viruses, Nature (London) **177**, 473 (1956).

[35] D. L. D. Caspar and A. Klug, Physical principles in the construction of regular viruses, Cold Spring Harbor Symp. **27**, 1 (1962).

[36] A. Klug, Architectural design of spherical viruses, Nature (London) **303**, 378 (1983).

[37] J. E. Johnson and J. A. Speir, Quasi-equivalent viruses: A paradigm for protein assemblies, J. Mol. Biol. **269**, 665 (1997).

[38] R. Zandi, D. Reguera, R. F. Bruinsma, W. M. Gelbart, and J. Rudnick, Origin of icosahedral symmetry in viruses, Proc. Natl. Acad. Sci. USA **101**, 15556 (2004).

[39] B. Stephanidis, S. Adichtchev, P. Gouet, A. McPherson, and A. Mermet, Elastic properties of viruses, Biophys. J. **93**, 1354 (2007).

[40] N. Zauberman, Y. Mutsafi, D. B. Halevy, E. Shimoni, E. Klein, C. Xiao, S. Sun, and A. Minsky, Distinct DNA exit and packaging portals in the virus *Acanthamoeba polyphaga mimivirus*, PLoS Biol. **6**, e114 (2008).

[41] R. V. Mannige and C. L. Brooks III, Periodic table of virus capsids: implications for natural selection and design, PLoS ONE **5**, e9423 (2010).

[42] E. R. May and C. L. Brooks III, Determination of Viral Capsid Elastic Properties from Equilibrium Thermal Fluctuations, Phys. Rev. Lett. **106**, 188101 (2011).

[43] A. Ahadi, D. Johansson, and A. Evilevitch, Modeling and simulation of the mechanical response from nanoindentation test of DNA-filled viral capsids, J. Biol. Phys. **39**, 183 (2013).

[44] R. F. Bruinsma and W. S. Klug, Physics of viral shells, Annu. Rev. Condens. Matter Phys. **6**, 245 (2015).

[45] S. Li, P. Roy, A. Travesset, and R. Zandi, Why large icosahedral viruses need scaffolding proteins, Proc. Natl. Acad. Sci. USA **115**, 10971 (2018).

[46] I. L. Ivanovska, P. J. de Pablo, B. Ibarra, G. Sgalari, F. C. MacKintosh, J. L. Carrascosa, C. F. Schmidt, and G. J. L. Wuite, Bacteriophage capsids: Tough nanoshells with complex elastic properties, Proc. Natl. Acad. Sci. USA **101**, 7600 (2004).

[47] W. S. Klug, R. F. Bruinsma, J.-P. Michel, C. M. Knobler, I. L. Ivanovska, C. F. Schmidt, and G. J. L. Wuite, Failure of Viral Shells, Phys. Rev. Lett. **97**, 228101 (2006).

[48] W. H. Roos, I. L. Ivanovska, A. Evilevitch, and G. J. L. Wuite, Viral capsids: mechanical characteristics, genome

packaging and delivery mechanisms, Cell. Mol. Life Sci. **64**, 1484 (2007).
[49] A. Arkhipov, W. H. Roos, G. J. L. Wuite, and K. Schulten, Elucidating the mechanism behind irreversible deformation of viral capsids, Biophys. J. **97**, 2061 (2009).
[50] G. A. Vliegenthart and G. Gompper, Mechanical deformation of spherical viruses with icosahedral symmetry, Biophys. J. **91**, 834 (2006).
[51] M. Buenemann and P. Lenz, Mechanical limits of viral capsids, Proc. Natl. Acad. Sci. USA **104**, 9925 (2007).
[52] M. M. Gibbons and W. S. Klug, Nonlinear finite-element analysis of nanoindentation of viral capsids, Phys. Rev. E **75**, 031901 (2007).
[53] M. G. Mateu, Mechanical properties of viruses analyzed by atomic force microscopy: a virological perspective, Virus Res. **168**, 1 (2012).
[54] M. Cieplak and M. O. Robbins, Nanoindentation of 35 virus capsids in a molecular model: relating mechanical properties to structure, PLoS ONE **8**, e63640 (2013).
[55] M. Marchetti, G. J. L. Wuite, and W. H. Roos, Atomic force microscopy observation and characterization of single virions and virus-like particles by nano-indentation, Curr. Opin. Virology **18**, 82 (2016).
[56] G. Bealle, J. Jestin, and D. Carriere, Mechanical properties of viruses analyzed by atomic force microscopy: A virological perspective, Soft Matter **7**, 1084 (2011).
[57] M. Krieg *et al.*, Atomic force microscopy-based mechanobiology, Nat. Rev. Phys. **1**, 41 (2019).
[58] C. Carrasco *et al.*, Built-in mechanical stress in viral shells, Biophys. J. **100**, 1100 (2011).
[59] A. Nasto, A. Ajdari, A. Lazarus, A. Vaziric and P. M. Reis, Localization of deformation in thin shells under indentation, Soft Matter **9**, 6796 (2013).
[60] A. Siber and R. Podgornik, Stability of elastic icosadeltahedral shells under uniform external pressure: Application to viruses under osmotic pressure, Phys. Rev. E **79**, 011919 (2009).
[61] S. Knoche and J. Kierfeld, Buckling of spherical capsules, Phys. Rev. E **84**, 046608 (2011).
[62] E. Couturier, J. Dumais, E. Cerda, and E. Katifori, Folding of an opened spherical shell, Soft Matter **9**, 8359 (2013).
[63] R. F. Bruinsma, W. M. Gelbart, D. Reguera, J. Rudnick, and R. Zandi, Viral Self-Assembly As a Thermodynamic Process, Phys. Rev. Lett. **90**, 248101 (2003).
[64] R. Zandi and D. Reguera, Mechanical properties of viral capsids, Phys. Rev. E **72**, 021917 (2005).
[65] P. van der Schoot and R. Bruinsma, Electrostatics and the assembly of an RNA virus, Phys. Rev. E **71**, 061928 (2005).
[66] T. T. Nguyen, R. F. Bruinsma, and W. M. Gelbart, Elasticity theory and shape transitions of viral shells, Phys. Rev. E **72**, 051923 (2005).
[67] T. T. Nguyen, R. F. Bruinsma, and W. M. Gelbart, Continuum Theory of Retroviral Capsids, Phys. Rev. Lett. **96**, 078102 (2006).
[68] A. Siber, Buckling transition in icosahedral shells subjected to volume conservation constraint and pressure: Relations to virus maturation, Phys. Rev. E **73**, 061915 (2006).
[69] A. Siber and R. Podgornik, Role of electrostatic interactions in the assembly of empty spherical viral capsids, Phys. Rev. E **76**, 061906 (2007).
[70] T. Guerin and R. Bruinsma, Theory of conformational transitions of viral shells, Phys. Rev. E **76**, 061911 (2007).
[71] M. Buenemann and P. Lenz, Elastic properties and mechanical stability of chiral and filled viral capsids, Phys. Rev. E **78**, 051924 (2008).
[72] C. A. Haselwandter and R. Phillips, Minimal Bending Energies of Bilayer Polyhedra, Phys. Rev. Lett. **105**, 228101 (2010).
[73] A. Siber, R. Zandi, and R. Podgornik, Thermodynamics of nanospheres encapsulated in virus capsids, Phys. Rev. E **81**, 051919 (2010).
[74] A. L. Bozic, A. Siber, and R. Podgornik, Statistical analysis of sizes and shapes of virus capsids and their resulting elastic properties, J. Biol. Phys. **39**, 215 (2013).
[75] M. F. Hagan, Modeling viral capsid assembly, Adv. Chem. Phys. **155**, 1 (2014).
[76] C. A. Haselwandter and R. Phillips, Elastic energy of polyhedral bilayer vesicles, Phys. Rev. E **83**, 061901 (2011).
[77] T. Tarnai and Z. S. Gaspar, Packing of equal regular pentagons on a sphere, Proc. R. Soc. A **457**, 1043 (2001).
[78] M. J. Bowick, A. Cacciuto, D. R. Nelson, and A. Travesset, Crystalline particle packings on a sphere with long-range power-law potentials, Phys. Rev. B **73**, 024115 (2006).
[79] A. L. Bozic and A. Siber, Electrostatics-driven inflation of elastic icosahedral shells as a model for swelling of viruses, Biophys. J. **115**, 822 (2018).
[80] R. Konecny, J. Trylska, F. Tama, D. Zhang, N. A. Baker, C. L. Brooks III, and J. A. McCammon, Electrostatic properties of Cowpea Chlorotic Mottle Virus and Cucumber Mosaic Virus capsids, Biopolymers **82**, 106 (2006).
[81] P. L. Freddolino, A. S. Arkhipov, S. B. Larson, A. McPherson, and K. Schulten, Molecular dynamics simulations of the complete satellite Tobacco Mosaic Virus, Structure **14**, 437 (2006).
[82] H. D. Nguyen, V. S. Reddy, and C. L. Brooks III, Deciphering the kinetic mechanism of spontaneous self-assembly of icosahedral capsids, Nano Lett. **7**, 338 (2007).
[83] G. Vernizzi, R. Sknepnek, and M. O. de la Cruz, Platonic and Archimedean geometries in multicomponent elastic membranes, Proc. Natl. Acad. Sci. USA **108**, 4292 (2011).
[84] R. Sknepnek, G. Vernizzi, and M. O. de la Cruz, Buckling of multicomponent elastic shells with line tension, Soft Matter **8**, 636 (2012).
[85] R. Sknepnek and M. O. de la Cruz, Nonlinear elastic model for faceting of vesicles with soft grain boundaries, Phys. Rev. E **85**, 050501(R) (2012).
[86] S. Paquay, H. Kusumaatmaja, D. J. Wales, R. Zandi, and P. van der Schoot, Energetically favoured defects in dense packings of particles on spherical surfaces, Soft Matter **12**, 5708 (2016).
[87] Z. Yao, R. Sknepnek, C. K. Thomas, and M. O. de la Cruz, Shapes of pored membranes, Soft Matter **8**, 11613 (2012).
[88] C. M. Funkhouser, R. Sknepnek, and M. O. de la Cruz, Topological defects in the buckling of elastic membranes, Soft Matter **9**, 60 (2013).
[89] V. Jadhao, C. K. Thomas, and M. O. de la Cruz, Topological defects in the buckling of elastic membranes, Proc. Natl. Acad. Sci. USA **111**, 12673 (2014).
[90] D. G. Angelescu and P. Linse, Viruses as supramolecular self-assemblies: Modeling of capsid formation and genome packaging, Soft Matter **4**, 1981 (2008).

[91] M. Zink and H. Grubmüller, Mechanical properties of the icosahedral shell of southern bean mosaic virus: a molecular dynamics study, Biophys. J. **96**, 1350 (2009).

[92] D. Wan, M. J. Bowick, and R. Sknepnek, Effects of scars on icosahedral crystalline shell stability under external pressure, Phys. Rev. E **91**, 033205 (2015).

[93] H. D. Nguyen and C. L. Brooks III, Generalized structural polymorphism in self-assembled viral particles, Nano Lett. **8**, 4574 (2008).

[94] J. Paulose, G. A. Vliegenthart, G. Gompper, and D. R. Nelson, Fluctuating shells under pressure, Proc. Natl. Acad. Sci. USA **109**, 19551 (2012).

[95] J. Paulose and D. R. Nelson, Buckling pathways in spherical shells with soft spots, Soft Matter **9**, 8227 (2013).

[96] J. Wagner and R. Zandi, The robust assembly of small symmetric nanoshells, Biophys. J. **109**, 956 (2015).

[97] A. R. Singh, L. E. Perotti, R. F. Bruinsma, J. Rudnick, and W. S. Klug, Ground state instabilities of protein shells are eliminated by buckling, Soft Matter **13**, 8300 (2017).

[98] J. B. Bancroft, E. Hiebert, M. W. Rees, and R. Markham, Properties of Cowpea Chlorotic Mottle Virus, its protein and nucleic acid, Virology **34**, 224 (1968).

[99] J. B. Bancroft, The self-assembly of spherical plant viruses, Adv. Virus Res. **16**, 99 (1970).

[100] P. A. Thuman-Commike, B. Greene, J. A. Malinski, J. King, and W. Chiu, Role of the scaffolding protein in P22 procapsid size determination suggested by $T = 4$ and $T = 7$ procapsid structures, Biophys. J. **74**, 559 (1998).

[101] M. A. Krol, N. H. Olson, J. Tate, J. E. Johnson, T. S. Baker, and P. Ahlquist, RNA-controlled polymorphism in the *in vivo* assembly of 180-subunit and 120-subunit virions from a single capsid protein, Proc. Natl. Acad. Sci. USA **96**, 13650 (1999).

[102] A. Zlotnick, J. M. Johnson, P. W. Wingfield, S. J. Stahl, and D. Endres, A theoretical model successfully identifies features of Hepatitis B Virus capsid assembly, Biochemistry **38**, 14644 (1999).

[103] P. Ceres and A. Zlotnick, Weak protein-protein interactions are sufficient to drive assembly of Hepatitis B Virus capsids, Biochemistry **41**, 11525 (2002).

[104] A. Zlotnick, Are weak protein-protein interactions the general rule in capsid assembly? Virology **315**, 269 (2003).

[105] M. G. Mateu, Assembly, stability and dynamics of virus capsids, Arch. Biochem. Biophys. **531**, 65 (2013).

[106] M. A. Greenfield, L. C. Palmer, G. Vernizzi, M. O. de la Cruz, and S. I. Stupp, Buckled membranes in mixed-valence ionic amphiphile vesicles, J. Am. Chem. Soc. **131**, 12030 (2009).

[107] A. Fery and R. Weinkamer, Mechanical properties of micro- and nanocapsules: single-capsule measurements, Polymer **48**, 7221 (2007).

[108] T. Rümenapf *et al.*, Aura Alphavirus subgenomic RNA is packaged into virions of two sizes, J. Virol. **69**, 1741 (1995).

[109] L. Lavelle *et al.*, Phase diagram of self-assembled viral capsid protein polymorphs, J. Phys. Chem. B **113**, 3813 (2009).

[110] M. Baclayon, G. J. L. Wuite, and W. H. Roos, Imaging and manipulation of single viruses by atomic force microscopy, Soft Matter **6**, 5273 (2010).

[111] S. S. Datta, S.-H. Kim, J. Paulose, A. Abbaspourrad, D. R. Nelson, and D. A. Weitz, Delayed Buckling and Guided Folding of Inhomogeneous Capsules, Phys. Rev. Lett. **109**, 134302 (2012).

[112] M. Brojan, D. Terwagne, R. Lagrange, and P. M. Reis, Wrinkling crystallography on spherical surfaces, Proc. Natl. Acad. Sci. USA **112**, 14 (2015).

[113] S. Bajaj and M. Banerjee, *In vitro* assembly of polymorphic virus-like particles from the capsid protein of a nodavirus, Virology **496**, 106 (2016).

[114] A plethora of statistical-mechanic problems have been posed and resolved over the last decades regarding the thermodynamics and energetics of the viral-capsid assembly as well as the peculiarities of genome packaging inside and DNA ejection from the capsids. Statistical mechanics and melting transitions of thin crystalline spherical shells at finite temperatures in the presence of fluctuations [42] were recently examined [118,119]. Fluctuating shells under pressure were also studied [94]. Still, the statistical mechanics and thermodynamics of virus-capsid formation are not fully understood.

[115] Single-stranded RNA viruses often have softer and not perfectly regular shells (see Ref. [120] for a classification of capsid proteins). For a number of double-stranded DNA viruses, and bacteriophages in particular, in contradistinction, empty capsids are formed first, while the DNA is packaged inside these protein nanocontainers later, by portal motor proteins. During this process, high effective pressures (of up to tens of atmospheres) are maintained inside the capsids [25].

[116] Double-stranded-DNA-based viruses more often have "edgy or faceted" icosahedral shells, vital to withstand the internal repulsive electrostatic and hydration pressure [33] (see Ref. [9] for an overview of structural organization and functioning mechanisms of (single- and double-stranded) DNA versus RNA viruses, membrane-enveloped versus nonenveloped viruses, etc.). The latter stems from closely proximal, often locally nearly parallel, juxtaposed DNA fragments in the DNA "spool" being formed inside the capsid. Bacteriophage capsids withstand external deformations extremely well: for instance, the respective Young's moduli for the λ-phage and $\phi 29$-phage prohead were measured [25,46,57,58] to be $\approx 1 \ldots 2$ GPa (reaching those of hard plastics; the majority of viral capsids are, however, substantially softer (roughly one to two orders of magnitude [58,79]). This second situation, when the capsids are formed prior to encapsidation of the genetic material, embodies a set of relevant biological systems for the analytical model considered below.

[117] Note that plastic or irreversible deformations of viral shells with comparatively small Young's moduli in nanoindentation experiments are realized at larger degrees of squeezing, while hard bacteriophage capsids are often brittle and prone to fracture [25]. From the initial slope of the force-indentation curve (the linear regime) the elastic spring constant of anisotropic viral capsids can be extracted [55] (along a given axis of the applied force [58]).

[118] A. Kosmrlj and D. R. Nelson, Statistical Mechanics of Thin Spherical Shells, Phys. Rev. X **7**, 011002 (2017).

[119] A. R. Singh, A. Kosmrlj, and R. Bruinsma, Finite Temperature Phase Behavior of Viral Capsids as Oriented Particle Shells, Phys. Rev. Lett. **124**, 158101 (2020).

[120] M. Krupovic and E. V. Koonin, Multiple origins of viral capsid proteins from cellular ancestors, Proc. Natl. Acad. Sci. USA **114**, E2401 (2017).

[121] A. Föppl, *Vorlesungen über Technische Mechanik V* (Teubner, Leipzig, 1907), pp. 132–144.
[122] T. von Kármán, *The Collected Works of Theodore von Kármán* (Butterworths, London, 1956), Vol. 1, p. 176.
[123] A. P. S. Selvadurai, *Partial Differential Equations in Mechanics: The Biharmonic Equation, Poisson's Equation*, Vol. 2 (Springer, Berlin, 2000).
[124] D. R. Nelson and L. Peliti, Fluctuations in membranes with crystalline and hexatic order, J. Phys. **48**, 1085 (1987).
[125] M. Widom, J. Lidmar, and D. R. Nelson, Soft modes near the buckling transition of icosahedral shells, Phys. Rev. E **76**, 031911 (2007).
[126] T. A. Witten and H. Li, Asymptotic shape of a fullerene ball, Europhys. Lett. **23**, 51 (1993).
[127] E. M. Kramer and T. A. Witten, Stress Condensation in Crushed Elastic Manifolds, Phys. Rev. Lett. **78**, 1303 (1997).
[128] T. Liang and T. Witten, Spontaneous curvature cancellation in forced thin sheets, Phys. Rev. E **73**, 046604 (2006).
[129] J. W. Wang and T. A. Witten, Compensation of Gaussian curvature in developable cones is local, Phys. Rev. E **80**, 046610 (2009).
[130] B. A. DiDonna and T. A. Witten, Anomalous Strength of Membranes with Elastic Ridges, Phys. Rev. Lett. **87**, 206105 (2001).
[131] B. Roman and A. Pocheau, Stress Defocusing in Anisotropic Compaction of Thin Sheets, Phys. Rev. Lett. **108**, 074301 (2012).
[132] A. Lobkovsky, S. Gentges, H. Li, D. Morse, and T. A. Witten, Scaling properties of stretching ridges in a crumpled elastic sheet, Science **270**, 1482 (1995).
[133] A. E. Lobkovsky, Boundary layer analysis of the ridge singularity in a thin plate, Phys. Rev. E **53**, 3750 (1996).
[134] A. E. Lobkovsky, Structure of crumpled thin elastic membranes, Ph.D. thesis, University of Chicago, 1996.
[135] A. E. Lobkovsky and T. A. Witten, Properties of ridges in elastic membranes, Phys. Rev. E **55**, 1577 (1997).
[136] E. Cerda, S. Chaieb, F. Melo, and L. Mahadevan, The distribution of Gaussian curvature in developable cones (d-cones), Nature (London) **401**, 46 (1999).
[137] E. Cerda and L. Mahadevan, Conical Surfaces and Crescent Singularities in Crumpled Sheets, Phys. Rev. Lett. **80**, 2358 (1998).
[138] M. M. Müller, M. Ben Amar, and J. Guven, Conical Defects in Growing Sheets, Phys. Rev. Lett. **101**, 156104 (2008).
[139] Y. Chushak and A. Travesset, Solid domains in lipid vesicles and scars, Europhys. Lett. **72**, 767 (2005).
[140] S. Knoche and J. Kierfeld, Secondary polygonal instability of buckled spherical shells, Europhys. Lett. **106**, 24004 (2014).
[141] S. Knoche and J. Kierfeld, Osmotic buckling of spherical capsules, Soft Matter **10**, 8358 (2014).
[142] Y. Kantor and D. R. Nelson, Phase transitions in flexible polymeric surfaces, Phys. Rev. A **36**, 4020 (1987).
[143] M. Ben Amar and Y. Pomeau, Crumpled paper, Proc. R. Soc. A **453**, 41 (1997).
[144] G. A. Vliegenthart and G. Gompper, Forced crumpling of self-avoiding elastic sheets, Nat. Mater. **5**, 216 (2006).
[145] T. Tallinen, J. A. Astrom, and J. Timonen, The effect of plasticity in crumpling of thin sheets, Nat. Mater. **8**, 25 (2009).
[146] K. Matan, R. B. Williams, T. A. Witten, and S. R. Nagel, Crumpling a Thin Sheet, Phys. Rev. Lett. **88**, 076101 (2002).
[147] O. Gottesman, J. Andrejevic, C. H. Rycroft, and S. M. Rubinstein, A state variable for crumpled thin sheets, Commun. Phys. **1**, 70 (2018).
[148] H. Diamant and T. A. Witten, Compression Induced Folding of A Sheet: An integrable System, Phys. Rev. Lett. **107**, 164302 (2011).
[149] G. A. Vliegenthart and G. Gompper, Compression, crumpling and collapse of spherical shells and capsules, New J. Phys. **13**, 045020 (2011).
[150] M. D. Emanuel, H. Mohrbach, M. Sayar, H. Schiessel, and I. M. Kulic, Buckling of stiff polymers: influence of thermal fluctuations, Phys. Rev. E **76**, 061907 (2007).
[151] J. Genzer and J. Groenewold, Soft matter with hard skin: From skin wrinkles to templating and material characterization, Soft Matter **2**, 310 (2006).
[152] L. Pocivavsek, R. Dellsy, A. Kern, S. Johnson, B. Lin, K. Y. C. Lee, and E. Cerda, Stress and fold localization in thin elastic membranes, Science **320**, 912 (2008).
[153] G. Gompper and D. M. Kroll, Statistical mechanics of membranes: freezing, undulations, and topology fluctuations, J. Phys.: Condens. Matter **12**, A29 (2000).
[154] G. Gompper and D. M. Kroll, Network models of fluid, hexatic and polymerized membranes, J. Phys.: Condens. Matter **9**, 8795 (1997).
[155] G. Gompper and D. M. Kroll, Triangulated-surface models of fluctuating membranes, in *Statistical Mechanics of Membranes and Surfaces*, edited by D. R. Nelson, T. Piran, and S. Weinberg, 2nd ed. (World Scientific, Singapore, 2004), Chap. 12, pp. 359–426.
[156] E. Cerda, K. Ravi-Chandar, and L. Mahadevan, Wrinkling of an elastic sheet under tension, Nature (London) **419**, 579 (2002)
[157] J. Huang, M. Juszkiewicz, W. H. de Jeu, E. Cerda, T. Emrick, N. Menon, and T. P. Russell, Capillary wrinkling of floating thin polymer films, Science **317**, 650 (2007).
[158] H. Vandeparre, M. Pineirua, F. Brau, B. Roman, J. Bico, C. Gay, W. Bao, C. N. Lau, P. M. Reis, and P. Damman, Wrinkling Hierarchy in Constrained Thin Sheets from Suspended Graphene to Curtains, Phys. Rev. Lett. **106**, 224301 (2011).
[159] J. Y. Chung, J. P. Youngblood, and C. M. Stafford, Anisotropic wetting on tunable micro-wrinkled surfaces, Soft Matter **3**, 1163 (2007).
[160] J. Hure, B. Roman, and J. Bico, Wrapping an Adhesive Sphere with An Elastic Sheet, Phys. Rev. Lett. **106**, 174301 (2011).
[161] B. Li, F. Jia, Y.-P. Cao, X.-Q. Feng, and H. Gao, Surface Wrinkling Patterns on a Core-Shell Soft Sphere, Phys. Rev. Lett. **106**, 234301 (2011).
[162] H. Noguchi and G. Gompper, Shape transitions of fluid vesicles and red blood cells in capillary flows, Proc. Natl. Acad. Sci. USA **102**, 14159 (2005).
[163] E. Katifori, S. Alben, E. Cerda, D. R. Nelson, and J. Dumais, Foldable structures and the natural design of pollen grains, Proc. Natl. Acad. Sci. USA **107**, 7635 (2010).
[164] F. Guinea, B. Horovitz, and P. Le Doussal, Gauge fields, ripples and wrinkles in graphene layers, Solid State Commun. **149**, 1140 (2009).
[165] M. Yamamoto, O. Pierre-Louis, J. Huang, M. S. Fuhrer, T. L. Einstein, and W. G. Cullen, "The Princess and the Pea" at the Nanoscale: Wrinkling and Delamination of Graphene on Nanoparticles, Phys. Rev. X **2**, 041018 (2012).

[166] On the softer end of the spectrum, the modes of deformation and dynamics of membranous vesicles (within the triangulated-network model in the presence of flows), as a model system mimicking the response and dynamics of red blood cells in microvascular flows, can also be mentioned [167,168]. Faceting of closed bilayer membrane vesicles of surfactant molecules is also well documented [20].

[167] D. A. Fedosov, M. Peltomäki, and G. Gompper, Deformation and dynamics of red blood cells in flow through cylindrical microchannels, Soft Matter **10**, 4258 (2014).

[168] M. Hoore, F. Yaya, T. Podgorski, C. Wagner, G. Gompper, and D. A. Fedosov, Effect of spectrin network elasticity on the shapes of erythrocyte doublets, Soft Matter **14**, 6278 (2018).

[169] A. M. Turner, V. Vitelli, and D. R. Nelson, Vortices on curved surfaces, Rev. Mod. Phys. **82**, 1301 (2010).

[170] Y. Mutsafi, N. Zauberman, I. Sabanay, and A. Minsky, Vaccinia-like cytoplasmic replication of the giant Mimivirus, Proc Natl. Acad. Sci. USA **107**, 5978 (2010).

[171] Y. Mutsafi, Y. Fridmann-Sirkis, E. Milrot, L. Hevroni, and A. Minsky, Infection cycles of large DNA viruses: Emerging themes and underlying questions, Virology **466-467**, 3 (2014).

[172] P. Lipowsky, M. J. Bowick, J. H. Meinke, D. R. Nelson, and A. R. Bausch, Direct visualization of dislocation dynamics in grain-boundary scars, Nat. Mater. **4**, 407 (2005).

[173] T. Einert, P. Lipowsky, J. Schilling, M. J. Bowick, and A. R. Bausch, Grain boundary scars on spherical crystals, Langmuir **21**, 12076 (2005).

[174] M. Bowick, H. Shin, and A. Travesset, Dynamics and instabilities of defects in two-dimensional crystals on curved backgrounds, Phys. Rev. E **75**, 021404 (2007).

[175] T. Kohyama and G. Gompper, Defect Scars on Flexible Surfaces with Crystalline Order, Phys. Rev. Lett. **98**, 198101 (2007).

[176] W. T. M. Irvine, M. J. Bowick, and P. M. Chaikin, Fractionalization of interstitials in curved colloidal crystals, Nat. Mater. **11**, 948 (2012).

[177] U. Seifert, Configurations of fluid membranes and vesicles, Adv. Phys. **46**, 13 (1997).

[178] R. Lipowsky and R. Dimova, Domains in membranes and vesicles, J. Phys.: Condens. Matter **15**, S31 (2003).

[179] J. Hu, T. Weikl, and R. Lipowsky, Vesicles with multiple membrane domains, Soft Matter **7**, 6092 (2011).

[180] S. Schneider and G. Gompper, Shapes of crystalline domains on spherical fluid vesicles, Europhys. Lett. **70**, 136 (2005).

[181] T. Baumgart, S. T. Hess, and W. W. Webb, Imaging coexisting fluid domains in biomembrane models coupling curvature and line tension, Nature (London) **425**, 821 (2003).

[182] E. Gutlederer, T. Gruhn, and R. Lipowsky, Polymorphism of vesicles with multi-domain patterns, Soft Matter **5**, 3303 (2009).

[183] F. Jülicher and R. Lipowsky, Domain-Induced Budding of Vesicles, Phys. Rev. Lett. **70**, 2964 (1993).

[184] T. Kohyama, D. M. Kroll, and G. Gompper, Budding of crystalline domains in fluid membranes, Phys. Rev. E **68**, 061905 (2003).

[185] C.-Y. Leung *et al.*, Molecular crystallization controlled by pH regulates mesoscopic membrane morphology, ACS Nano **6**, 10901 (2012).

[186] The phase diagram was rationalized in terms of the Gaussian curvature, the bending moduli, and the line tension λ between the coexisting phases on the surface. No effect of spontaneous membrane curvature was considered [182]. A variety of vesicles of prolate and oblate shapes with various numbers of flexible domains was found via numerical energy minimization [182]. The case of freely adjustable volume was examined, with no inside-outside pressure difference. The budding scenarios observed in real multicomponent vesicles [183] are indeed due to segregation of lipids into distinct domains [181] with different parameters that helps to minimize the total free energy.

[187] S. Tzlil, J. T. Kindt, W. M. Gelbart, and A. Ben-Shaul, Forces and pressures in DNA packaging and release from viral capsids, Biophys. J. **84**, 1616 (2003).

[188] P. K. Purohit, M. M. Inamdar, P. D. Grayson, T. M. Squires, J. Kondev, and R. Phillips, Forces during bacteriophage DNA packaging and ejection, Biophys. J. **88**, 851 (2005).

[189] A. J. Spakowitz and Z.-G. Wang, DNA packaging in bacteriophage: is twist important? Biophys. J. **88**, 3912 (2005).

[190] V. A. Belyi and M. Muthukumar, Electrostatic origin of the genome packing in viruses, Proc. Natl. Acad. Sci. USA **103**, 17174 (2006).

[191] C. Forrey and M. Muthukumar, Langevin dynamics simulations of genome packing in bacteriophage, Biophys. J. **91**, 25 (2006).

[192] D. Marenduzzo, E. Orlandini, A. Stasiak, D. W. Sumners, L. Tubiana, and C. Micheletti, DNA-DNA interactions in bacteriophage capsids are responsible for the observed DNA knotting, Proc. Natl. Acad. Sci. USA **106**, 22269 (2009).

[193] R. Podgornik, M. A. Aksoyoglu, S. Yasar, D. Svensek, and V. A. Parsegian, DNA equation of state: *in vitro* vs *in viro*, J. Phys. Chem. B **120**, 6051 (2016).

[194] S. J. de Calvalho, R. Metzler, and A. G. Cherstvy, Inverted critical adsorption of polyelectrolytes in confinement, Soft Matter **11**, 4430 (2015).

[195] A. G. Cherstvy, Shape morphologies of icosahedral two-component vesicles, J. Phys. Chem. B **121**, 7484 (2017).

[196] S. L. Veatch and S. L. Keller, Separation of liquid phases in giant vesicles of ternary mixtures of phospholipids and cholesterol, Biophys. J. **85**, 3074 (2003).

[197] M. Dubois, B. Deme, T. Gulik-Krzywicki, J.-C. Dedieu, C. Vautrin, S. Desert, E. Perez, and T. Zemb, Self-assembly of regular hollow icosahedra in salt-free catanionic solutions, Nature (London) **411**, 672 (2001).

[198] M. Dubois, V. Lizunov, A. Meister, T. Gulik-Krzywicki, J. M. Verbavatz, E. Perez, J. Zimmerberg, and T. Zemb, Shape control through molecular segregation in giant surfactant aggregates, Proc. Natl. Acad. Sci. USA **101**, 15082 (2004).

[199] The approximation of equidistantly positioned defects is consistent with the picture of long-range repulsion between topological defects as in the Coulomb-type gas. The results of computer simulations of the two-component vesicles can yield [83,84], however, clearly nonicosahedral forms and also possible coalescence of soft-component regions into larger nonsymmetric domains (depending on the model parameters).

[200] G. A. Vliegenthart (unpublished).

[201] The relation (14) will not hold for a strainless coverage of spherical domes since the dome circumferences will not match to create a smooth closed structure. Therefore, we interpret the *generalized dome* structure as slightly deformed. As long as the dome area stays constant, its strain energy does not change

dramatically. Likewise, if the solid angle covered by the dome stays constant, its bending energy also stays nearly constant.

[202] A. M. Kosevich, E. M. Lifshitz, L. D. Landau, and L. P. Pitaevskii, *Course of Theoretical Physics: Theory of Elasticity*, 3rd ed. (Butterworth-Heinemann, Oxford, 1986).

[203] B. Schmidt and F. Fraternali, Universal formulas for the limiting elastic energy of membrane networks, J. Mech. Phys. Solids **60**, 172 (2012).

[204] For large shells (within the realm of applicability of standard elasticity theory) this energy does not depend on the shell size. For very small shells, however, some variations in shell dimensions can potentially alter the defect-defect interaction energy and also the actual value of E_{core}. These situations are, however, well beyond the scope of our standard elasticity model applicable only to large shells. All these concepts are explained in detail in Ref. [14] (see also Refs. [11,45]).

[205] $\mathbf{cyls}_n$ is the tangent in the direction of the axis of a cylindrical segment. The tangent is of course a vector (on a two-dimensional surface like the cylindrical segment the tangent space is supported by a basis of two directions, for the cylindrical segment a natural choice is in the direction of the axis and orthogonal to this).

[206] For such surfaces, the first (tangent plane), but not the second derivative (continuous curvature) is realized. By choosing the surface to be developable, all Gaussian curvature (and, thus, the strain) are moved to the domes, with the rest of the surface being developable. We remind the reader that developable surfaces are only sections of cones, cylinders, are flat surfaces. This provides a partial justification and rationale for the parametrization of icosahedral shells used in our current analysis.

[207] The *edge sharpening* transitions often, however, feature small curvature radii. At such length scales the response might become nonelastic and irreversible and, as a consequence, the effective bending moduli in highly deformed regions might become comparable for the rigid and soft phases. Lastly, a finite intrinsic curvature of the material can reduce the elastic energy stored in a ridge.

[208] One still lacking ingredient is the strain in the edge. The cylindrical segment will have to sag because the length of an arc along the spherical surface from edge to edge is longer along the edge than along the center of the respective faces. This sagging comes with strain due to the Gaussian curvature. The "stiffer" the surface (the higher the FvK number), the larger the tendency to concentrate this sagging to a smaller stretch of the edge. This balances against the strain caused by compression if the edge would not sag at all. This idea could be a basis for an extended model that could explain or rationalize the scaling behaviors (70) and (71).

[209] The FvK number (7) follows from buckling from a sphere to 12 cones that energetically appears not to be the cheapest mode of deformations at the buckling transition. Geometrically and according to the v-cone model, the cheaper transition is to have cylindrical segments supported by flat faces, realized at $\beta_{\text{cyls}} = \beta_T$ and corresponding to lower buckling FvK number (74). When γ increases above γ_b the model turns into to the dome-cone model with $\beta_{\text{cyls}} = 0$ until some energy plateau appears (see Fig. 10). The ridges of Witten [132], with the energy scaling (9), appear, however, at significantly larger FvK numbers.

[210] In our approach for the single-component icosahedral shells, the radius of a spherical segment on top of each disclination cone is found self-consistently, so that the total elastic energy of the bent spherical domes and stretched cones smoothly connected to them is optimized. In the variable-cone model, the radius of the spherical dome unequivocally determines the radius of the cylindrical segments running along the edges of the v-cone. The inner cylindrical angle beta is found by the following adjustment. While $\beta = 0$ corresponds to a model of circular cones and immediately after buckling $\beta = \beta_T$ with the faces being flat, the optimal value of β is found via interpolating between $\beta = \beta_T$ and $\beta = 0$. It appears that expression (72) results in a nearly perfect fit and ensures energy optimization. The model of regular cones and spherical domes always yields the lowest elastic energy, but it does not fit the simulations of Lidmar *et al.* [18] accurately. The reason is that strains in the cones, and especially along the edges, are not included in the current model, but they do influence the cones regularity. We try to describe this geometric frustration by allocating a part of surface bending to the edges.

[211] Corrected as compared to Eq. (7) with $\gamma_b \approx 154$ via rescaling of the moduli (42) and (44) using Eq. (39).

[212] R. Waehler, S. J. Russell, and D. T. Curiel, Engineering targeted viral vectors for gene therapy, Nat. Rev. Genet. **8**, 573 (2007).

[213] B. Brandenburg and X. Zhuang, Virus trafficking learning from single-virus tracking, Nat. Rev. Microbiol. **5**, 197 (2007).

[214] M. V. de Ruiter, R. M. van der Hee, A. J. M. Driessen, E. D. Keurhorst, M. Hamid, and J. J. L. M. Cornelissen, Polymorphic assembly of virus-capsid proteins around DNA and the cellular uptake of the resulting particles, J. Contr. Release **307**, 342 (2019).

[215] W. Walther and U. Stein, Viral vectors for gene transfer: a review of their use in the treatment of human diseases, Drugs **60**, 249 (2000).

[216] P. Mancheno-Corvo and P. Martin-Duque, Viral gene therapy, Clin. Transl. Oncol. **12**, 858 (2006).

[217] Specifically, the amoeba-infecting *Acanthamoeba polyphaga* mimivirus (*mi*crobe-*mi*micking virus) belongs to a family of large internal-membrane-containing nucleocytoplasmic DNA viruses. The inner lipid membrane of these viruses forms an additional container for internalizing the genomic DNA. For the mimivirus virions, fully formed empty capsids are being formed first, while the DNA packaging into preassembled capsids takes place later. The DNA packing density is much smaller (about sixfold) than that inside a typical bacteriophage [218]. Contrary to the vertex-centered DNA-packing motors in bacteriophages and herpes viruses, the DNA encapsulation in mimiviruses takes place though an aperture in an icosahedral face opposite to the stargate [40].

[218] A. Minsky (private communication).

[219] For instance, for two proximal hexagonal subunits the interaction potentials along the side-to-side contact, mostly emerging from the buried hydrophobic protein surfaces and the release of water molecules of solvation, but also from the salt-dependent and sometimes pH-sensitive intersubunit electrostatic repulsive interactions [65,79,103,104], are not only varying azimuthally, but possibly also having a predisposed

angle of out-of-plane bending that optimizes the subunit-subunit association. This nonzero angle for a pair of subunits predetermines (to a certain extent) the preferred *mean intrinsic curvature* [109] and, ultimately, the preferred size of the resulting closed shell.

[220] Note also that the azimuthal deformations of viral-capsid subunits appear to yield larger elastic energy variations as compared to flexural out-of-plane bending of subunits along their contact line. This likely causes the shapes of large viral capsids to be polyhedral, similar to the faceting transition for giant fullerenes [7].

[221] This is the case, e.g., for small spherical single-stranded-RNA viruses such as Cowpea Chlorotic Mottle Virus (CCMV) [98,99]: polymorphic assembly takes place in the absence of RNA at non-native conditions or when the subunit-subunit interactions are modulated. The modulating factors are, e.g., the pH level, the ionic strength, the presence of certain divalent cations such as Mg^{2+} in the solution [governing also swelling [80,98,99] of CCMV (divalent cations potentially affect also the RNA compaction properties)], the scaffolding proteins regulating the size of some capsids [100], etc. We refer to the detailed study [99] on the structure and assembly of CCMV and other spherical plant viruses, both in the absence and presence of RNA. This "exceptional" virus has been thoroughly investigated and its protein subunits in the absence of RNA, depending on pH and salt concentration, self-assemble into a variety of structures, such as the planar sheets, single- and double-walled round-end tubules as well as single-wallede and multiwalled spherical shells [99,109]. Therefore, one can conclude that for the CCMV the interactions of the adjacent subunits are not very sensitive to relative orientations and dihedral angles between the subunits, thereby allowing for a variety of *polymorphic* capsid structures to realize. Moreover, other viral shells can also be enveloped by a layer of CCMV capsid proteins [99].

[222] R. Penrose, Pentaplexity: A class of non-periodic tilings of the plane, Math. Intelligencer **2**, 32 (1979).

[223] R. Twarock, A tiling approach to virus capsid assembly explaining a structural puzzle in virology, J. Theor. Biol. **226**, 477 (2004).

[224] K. S. Novoselov, V. I. Fal'ko, L. Colombo, P. R. Gellert, M. G. Schwab, and K. Kim, A roadmap for graphene, Nature (London) **490**, 192 (2012).

[225] C. Lee, X. Wei, J. W. Kysar, and J. Hone, Measurement of the elastic properties and intrinsic strength of monolayer graphene, Science **321**, 385 (2008).

[226] C. Soldano, A. Mahmood, and E. Dujardin, Production, properties and potential of graphene, Carbon **48**, 2127 (2010).

[227] J. Tersoff, Energies of fullerenes, Phys. Rev. B **46**, 15546 (1992).

[228] A. Siber, Energies of sp^2 carbon shapes with pentagonal disclinations and elasticity theory, Nanotechnology **17**, 3598 (2006).

[229] D. Bakowies, M. Biihl, and W. Thiel, Can large fullerenes be spherical? J. Am. Chem. Soc. **117**, 10113 (1995).

[230] C.-H. Xu and G. E. Scuseria, An O(N) tight-binding study of carbon clusters up to C8640: The geometrical shape of the giant icosahedral fullerenes, Chem. Phys. Lett. **262**, 219 (1996).

[231] P. Calaminici, G. Geudtner, and A. M. Köster, First-principle calculations of large fullerenes, J. Chem. Theory Comput. **5**, 29 (2009).

[232] R. R. Zope, T. Baruah, M. R. Pederson, and B. I. Dunlap, Static dielectric response of icosahedral fullerenes from C60 to C2160 characterized by an all-electron density functional theory, Phys. Rev. B **77**, 115452 (2008).